POLITECNICO DI TORINO

DEVELOPMENT OF A 3-DOF

SPHERICAL ACTUATOR

CANDIDATE:

SILVIO TISATO

SUPERVISOR:

PROF. **MICHELE ANGELO PASTORELLI**

ABSTRACT

Permanent magnet spherical actuators have seen an increase in interest due potential applications in areas like robotics, satellite control and sensors.

This work presents one such actuator, along with approaches to multi-dof actuation.

A review of relevant magnetic field equations is presented along with modelling methodologies. Selected existing designs are also presented: firstly, the ball-joint like design, which uses a single row of permanent magnets distributed along the equator. Then the deflection-type is presented, which comprises a rotor made up of the spherical tile permanent magnet, and the E-Shape stator design, which uses blade shaped back iron for the rotor to reduce weight, and finally an overview of a reaction sphere design for satellite attitude control is given, which used spherical top shaped permanent magnet positioned on the vertex of a dodecahedron.

The designed actuator is also presented, along with a 3D model and its magnetic and torque modelling, as well as comparison between the obtained magnetic flux density values with the ones obtained by means of FEM. Finally, some variations on the design are analysed.

INDEX

1 SPHERICAL MOTION

Spherical motion occurs frequently in many mechanical systems such as orientation mechanisms, robotic wrists, etc, and actuators that can produce multi-dof rotations in a single joint presents numerous potential applications in a variety of industries, such as robotics, advanced manufacturing, medical and automotive.

Spherical motion is the rotation of a system about a common point, the center of rotation, and it is characterized by an angle and an axis passing through the center of rotation.

Spherical motion generators can be categorized following different rules [1], for example by the mechanism by which the spherical motion is generated, by the actuation principle employed, or by the number of degrees of freedom they provide. Figure 1 shows one possible way to consider these categories.
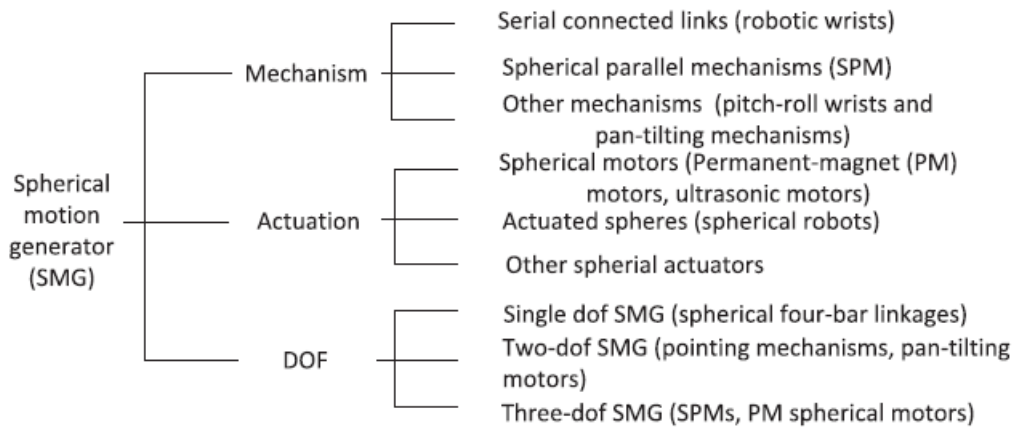
Figure 1 Categorization of SMG [1]

The simplest way spherical motion generators can be categorized is by actuation principle, dividing them into electromagnetic, piezoelectric and mechanically driven systems.

1.1 PIEZOELECTRIC

The piezoelectric effect converts an electrical stimulation into a mechanical actuation. This is possible thanks to the properties of some materials to produce a variation in the interatomic distance inside a crystal of material when its electrical equilibrium is altered by applying an external electric dipole. An example of piezoelectric material is PZT (lead zirconate titanate).

This kind of actuators is especially useful for camera modules and adaptive optics, as it allows to generate motions in the range of nanometers to millimiters. While conventional electromagnetic motors are more conventionally used for motion generation, at millimetre scales they show poor performances, and piezoelectric motors become competitive regarding power density, driving force and displacement resolution when compared to conventional electromagnetic micromotors.

Piezoelectric motors are thus good candidates for use in micro-mechanical system that need high precision, for example in surgical devices or joint in robot manipulators.

Figure 2 shows one proposed piezoelectric actuator for surgical use[2]. It is a type of ultrasonic spherical motor, with a bar-shaped piezoelectric stator and a sphere-shaped rotor. The three natural vibrations of the stator allow it to move the rotor. The rotations around the axes are given by combining bending and/or translation modes of the stator, for example rotation around the z-axis is obtained by combining the bending mode on plane xz and yz, while the rotation around the x-axis is obtained by combining the longitudinal mode along the z axis and the bending mode in the yz plane.
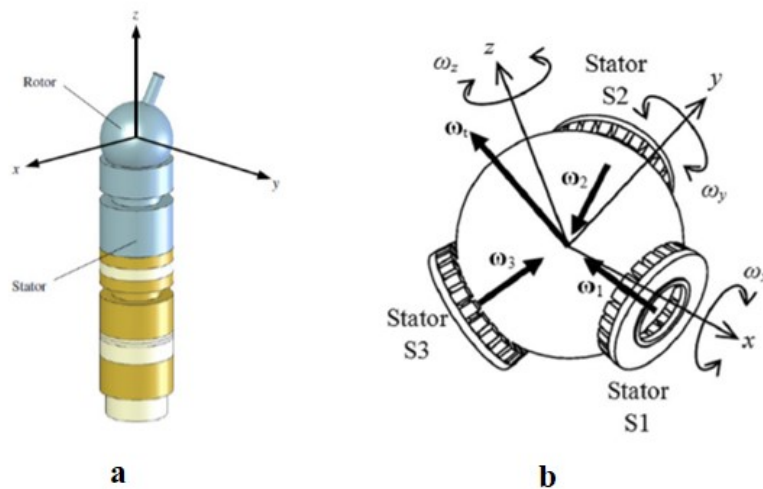
Figure 2 (a) Piezoelectric actuator for surgical use and (b) multi-stator spherical motion motor

Another kind of spherical motion motor that employs the piezoelectric effect can be seen in Figure 2. It is composed of three ring shaped piezoelectric ultrasonic stators and a spherical rotor[3]. The angular velocity of the motor is determined by combining the angular velocities produced by the three stators. This kind of motor is promising as an alternative to servomotor-based gimbals.

1.2 MECHANICALLY DRIVEN
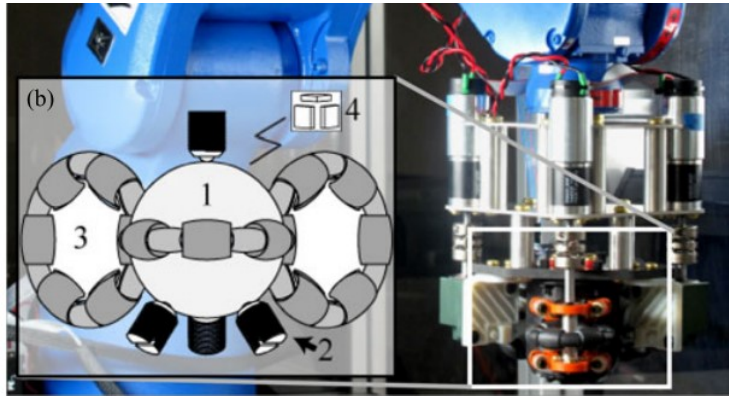
Figure 3 Wheel-driven spherical actuator

Mechanically driven spherical motors are usually obtained by multiple single degree of freedom motors in series or parallel.

One such motor is shown in Figure 3 above. This motor is called SAMM[4] and presents three single degree of freedom motors connected to wheels, and these wheels produce a contact force on a sphere, producing the spherical motion. This kind of system have the disadvantage of being structurally complex and also dissipating energy by friction between the wheel and the sphere. The weight of the wheels and the sphere also decreases the motion dexterity of the system due to inertial effects.

Note that the wheels are omniwheels, as they incorporate rollers such that they allow free rotation on the axes perpendicular to the main wheel axis, which can be controlled.

Another kind of mechanically driven motor is the one called wire-driven spherical motor[5]. This motor presents wires attached to a sphere. By acting on the wires, spherical motion can be achieved.
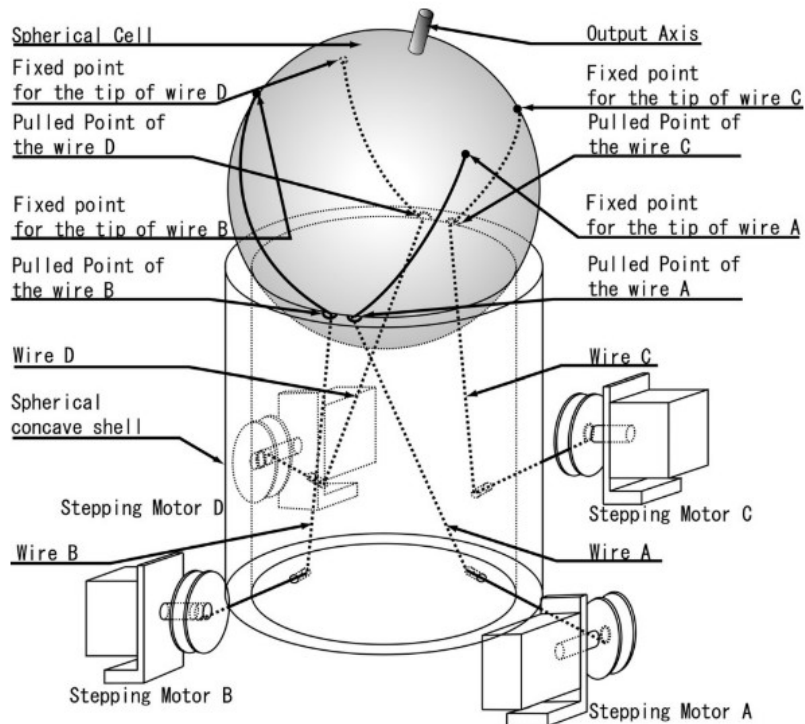
Figure 4 wire-driven spherical actuator

1.2.1 Electromagnetic

Electromagnetic spherical motors obtain the spherical motion by electromagnetism. Some examples are induction, DC, stepper and permanent magnets based motors.

Electromagnetic spherical motors are the main topic of this work, and as such they will be discussed in more details in the following chapters.

This category can be further broken down subdividing the electromagnetic spherical motors by the working principle they employ[6]:

- Orthogonal type
- Stepping type
- Tiered type
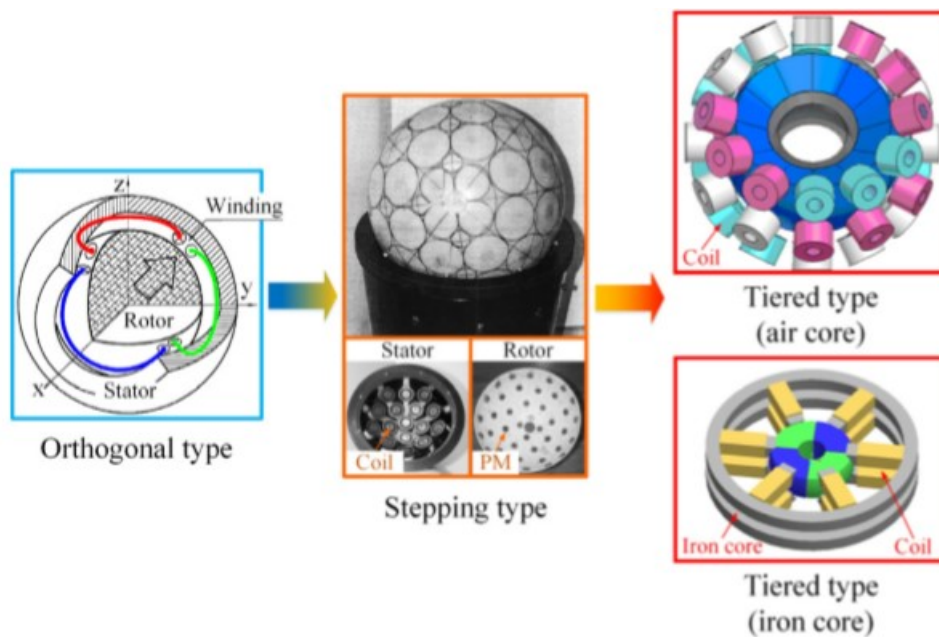
Figure 5 Types of spherical motors[6]

Orthogonal type motors employ windings orthogonal to each other, producing a 3D rotating electromagnetic field.

Stepping type motors have a very high number of rotor poles and stator coils, usually symmetrically distributed.

Tiered type motors have multiple layers of stator coils or rotor permanent magnet poles, distributed evenly. The coils in the stator may be air or iron cored.

Tiered type motors usually only allow a limited range of tilt angle, while allowing continuous spinning rotation. For this reason, they are more suited for applications such as machine tools.

2 SPHERICAL PM ACTUATORS

Magnetic actuators are a class of devices that include various technologies. Actuators that can achieve 3-DOF motion are increasingly used in industry. These kinds of devices are usually built with multiple conventional motors, each adding one DOF, reducing the position accuracy, efficiency and dynamic performance of the system. For these reasons, multi-DOF actuators have received growing interest, however their operating mechanism and control algorithm are of course very different from 1-DOF ones. Spherical actuators, a type of magnetic actuators, have the advantage of compact size and high precision motion and can provide multi-DOF motion. They can assume very different forms, like induction, reluctance, ultrasonic and more. The most commonly used kind is reluctance spherical actuators thanks to their relative simplicity and compactness, but they present problem like nonlinear rotor dynamics, complex magnetic field and complicated actuating system.

The air-gap magnetic field is a determinant quantity for predicting the performance of a magnetic actuator, and to optimize actuator performance an analytical model of the magnetic field must be established, as despite the advancements in computing power, using techniques such as finite element method (FEM) is still too time consuming and doesn't easily allow for parametric design studies.

2.1 FUNDAMENTAL EQUATIONS

The electromagnetic behaviour for devices with permanent magnets can be described starting with Maxwell's Equations, which in differential form can be stated as

$$\nabla \times H = J + \frac{\partial D}{\partial t} \tag{2.1}$$

$$\nabla \cdot B = 0 \tag{2.2}$$

$$\nabla \times E = -\frac{\partial B}{\partial t} \tag{2.3}$$

$$\nabla \cdot D = \rho_c \tag{2.4}$$

And the equations

$$B = \mu_0(H + M) \tag{2.5}$$

$$D = \varepsilon_0 E + P \tag{2.6}$$

$$J = \sigma_e E \tag{2.7}$$

The flux density can be written as

$$B = \mu_0 H + B_r \tag{2.8}$$

Since we consider a magnetostatics case, in which field changes are assumed to happen instantaneously, the term $\partial D/\partial t$ is negligible and so

$$\nabla \times H = J \tag{2.9}$$

$$\nabla \cdot B = 0 \tag{2.10}$$

We can state the field equation as Poisson's Equation

$$\nabla^2 \varphi = f \tag{2.11}$$

Which in magnetization free regions becomes known as Laplace's Equation:

$$\nabla^2 \varphi = 0 \tag{2.12}$$

2.2 MAGNETIC FIELD ANALYTICAL MODELS

2.2.1 Magnetic Equivalent Charge Model

The magnetic charge model can be used to obtain the spatial distribution of the magnetic flux density produced by permanent magnet arrays. In this model, the permanent magnets are replaced by an equivalent distribution of "magnetic charges", and this charge distribution is used as a source term in the magnetostatics field equations

$$\nabla \times H = 0 \qquad \qquad 2.13$$
$$\nabla \times B = 0 \qquad \qquad 2.14$$

In the case of spherical permanent magnet, first a complete solution for the spherical tile is calculated, and then thanks to the superposition principle the magnetic flux density of the spherical magnet array is obtained. In the following, it is assumed that the permanent magnets are uniformly magnetized and have a relative permeability of $\mu_r = 1$. With this assumption, a small error is made because permanent magnets usually have a relative permeability in the order of 1.03–1.05.

The flux density can be written as

$$B = \mu_0 H + B_r = \mu_0 H + M \qquad \qquad 2.15$$
$$B = -\mu_0 \nabla \varphi_m + M \qquad \qquad 2.16$$

The magnetic scalar potential can be written as [7]

$$\varphi_m = \frac{1}{4\pi} \int_V \frac{\rho_m}{|x - x'|} dv' + \frac{1}{4\pi} \oint_S \frac{\sigma_m}{|x - x'|} ds' \qquad \qquad 2.17$$

$$\rho_m = -\nabla \cdot M = \frac{2}{r'} M_0$$
$$\sigma_m = M \cdot \hat{n}$$
$$x = (r, \theta, \varphi) \, ; x' = (r', \theta', \varphi')$$
$$|x - x'| = \sqrt{r^2 + r'^2 - 2\, r\, r'(\sin \theta \sin \theta' \cos(\varphi - \varphi') + \cos \theta \cos \theta')}$$

Using the Maxwell equations together with the constitutive relation $B = -\mu_0 \nabla \varphi_m + M$ the magnetic flux density field can be obtained as

$$B = -\mu_0 \nabla \left(\frac{1}{4\pi} \int_V \frac{\rho_m}{|x - x'|} dv' + \frac{1}{4\pi} \oint_S \frac{\sigma_m}{|x - x'|} ds' \right) \qquad \qquad 2.18$$

$$B = -\frac{\mu_0}{4\pi} \int_V \rho_m \nabla \frac{1}{|x - x'|} dv' + \frac{1}{4\pi} \oint_S \sigma_m \nabla \frac{1}{|x - x'|} ds' \qquad \qquad 2.19$$

2.2.2 Harmonic Expansion Model

Starting from the Laplace equation in spherical coordinates

$$\frac{1}{r^2} \frac{\partial}{\partial r} \left(r^2 \frac{\partial \varphi}{\partial r} \right) + \frac{1}{r^2 \sin \theta} \frac{\partial}{\partial \theta} \left(\sin \theta \frac{\partial \varphi}{\partial \theta} \right) + \frac{1}{r^2 \sin^2 \theta} \frac{\partial^2 \varphi}{\partial \phi^2} = 0 \qquad \qquad 2.20$$

The general solution is written as [8]

$$\varphi(r, \theta, \varphi) = \sum_{n=0}^{\infty} \sum_{m=-n}^{n} \left(C\, r^n + D\, r^{-(n+1)} \right) Y_n^m(\theta, \varphi) \qquad \qquad 2.21$$

$$\varphi(r, \theta, \varphi) = \sum_{n}^{\infty} \sum_{m=-n}^{n} \cdot \left(C \, r^n + D \, r^{-(n+1)} \right) S_n^m \, P_n^m(\cos \theta) e^{i \, m \, \varphi} \qquad 2.22$$

where S_n^m is

$$S_n^m = \sqrt{\frac{2n+1}{4\pi} \cdot \frac{(n-m)!}{(n+m)!}} \qquad 2.23$$

And $P_n^m(cos\theta)$ is the associated Legendre polynomial.

The radial component of the magnetization vector can be approximated using spherical harmonics[9]

$$M_r(\theta, \phi) = \sum_{n}^{\infty} \sum_{k}^{n} C_{nm} Y_n^m(\theta, \varphi) \qquad 2.24$$

Where the spherical harmonic coefficients can be obtained by

$$C_{nm} = \int_0^{2\pi} \int_0^{\pi} M_{0r}(\theta, \varphi) Y_n^{m*}(\theta, \varphi) \sin \theta \, d\theta d\varphi \qquad 2.25$$

Where Y_n^{m*} is the complex conjugate of the spherical harmonic Y_n^m.

By reordering the integral we get to

$$C_{nm} = \int_0^{2\pi} f(\varphi) e^{-i \, m \, \varphi} d\varphi \int_0^{\pi} S_n^m \, P_n^m(\cos \theta) \sin^2 \theta \, d\theta \qquad 2.26$$

By imposing boundary conditions, expressions for C and D parameters can be derived, with $C \equiv 0$ and $D = C_{nm} d_n$, so

$$\varphi(r, \theta, \varphi) = \sum_{n}^{\infty} \sum_{m=-n}^{n} C_{nm} d_n r^{-n-1} Y_n^m(\theta, \varphi) \qquad 2.27$$

And finally

$$B_{1r} = -\mu_0 \frac{\partial \varphi}{\partial r} = -\mu_0 \sum_{n}^{\infty} \sum_{m=-n}^{n} (-n-1) \cdot C_{nm} d_n r^{-n-2} Y_n^m(\theta, \varphi) \qquad 2.28$$

2.3 TORQUE ANALYTICAL MODEL - LORENTZ FORCE METHOD

Lorentz force is commonly defined as the combination of electric and magnetic force on a point charge due to electromagnetic fields, so considering a single charge q moving with speed v we have:

$$F = q\,E + q\,v \times B$$

For a continuous charge distribution, the equation becomes

$$dF = dq\,(E + v \times B)$$

Or dividing by the volume dV:

$$f = \rho(E + v \times B)$$

And since the we can write the current density as $J = \rho\,v$ we obtain the volume integral

$$F = \int_V (\rho E + J \times B)dV$$

And by using the definition of electric current I and considering a stationary wire, we can write

$$F = I \int_V d\ell \times B$$

The torque can be written as the cross product of the moment arm r and the force dF so

$$dT_i = r \times Id\ell \times B_r$$

And the torque generated by the i-th coil is then

$$T_i = \int_V r \times d\ell \times B_r dV$$

2.4 FINITE ELEMENT MODEL

2.4.1 Introduction to Ansys Maxwell

Ansys Maxwell is one of the leading electromagnetic field simulation softwares. It can be used to solve various kind of electromagnetic problems, such as electrostatic, magnetostatic and transients by using the Finite Element Method, both in 2D and 3D. This allows Maxwell to be used to perform design of electric motors, sensors, transformers and other electrical devices, reducing prototyping cost.

The major steps to perform an analysis with Ansys Maxwell are

- Choice of the problem type
- Definition of the geometry
- Definition of the material properties
- Definition of the excitations and boundaries
- Define parameters
- Analysis setup
- Post processing

Maxwell uses different solvers for different problem types. Some examples are static, transient, eddy current.
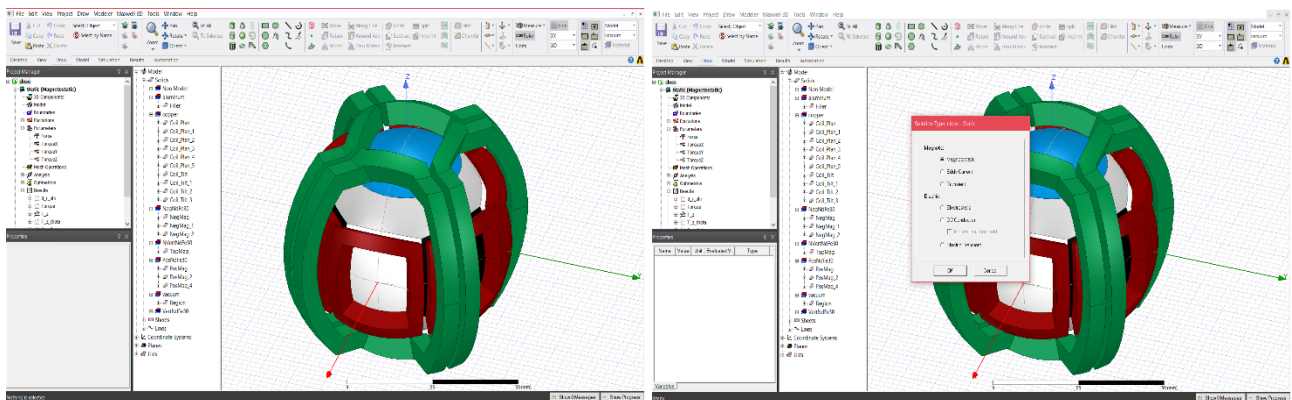
Figure 6 General View (left) Solution Type Selection window (right)

The problem can be defined either as 2D or 3D geometry, drawn directly with Maxwell or imported from common CAD or 3D modelling software. In particular, Maxwell 3D modeller makes uses of Boolean geometry to define the structure, as the geometry is made up basic "block" like cylinders or boxes that are combined into single entities by Boolean operations like unite, subtract, intersect etc.

Material properties can be assigned to every body via the properties window, and they can be chosen either from the extensive built in material library or added as custom materials. For magnetic materials, its also possible to define the B-H cure by imputing points.

Excitations can be defined either as voltage, current or permanent magnet, while boundary condition can be for example symmetry, tangential H field, insulating, etc.

Maxwell can solve for most common parameters, like torque, force and inductance.

The analysis setup defines the number of passes and the percentage of error allowed, as well as the mesh refinement to be performed after each pass.
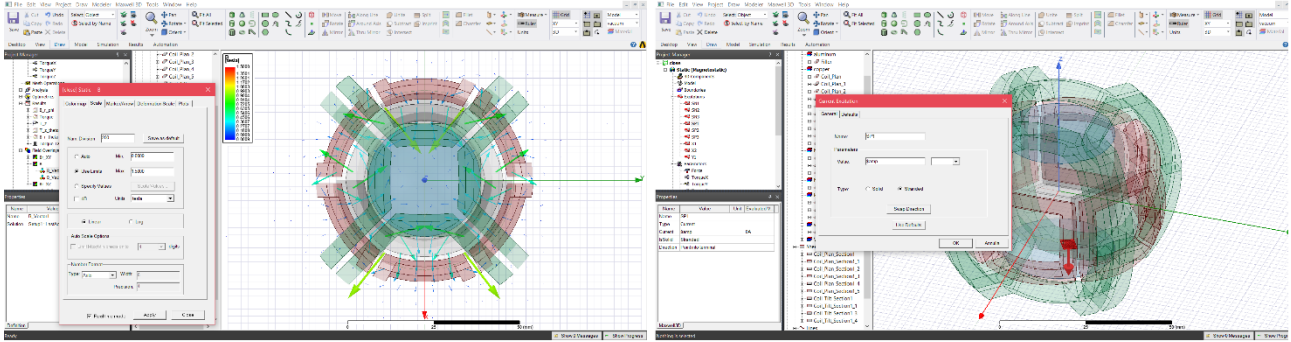
Figure 7 Post processing graph options (left) Excitation configuration (right)

After running the simulation, different kinds of solution graphs can be obtained by post processing the results. Some example are B and H-field density or vector plots.

2.4.2   Maxwell FEM formulation

Finite Element Analysis can be performed using various different electromagnetic field formulations to solve Maxwell's equations. The one used in Ansys Maxwell starts from the basic field equations

$$\nabla \times E = -\frac{\partial B}{\partial t} \qquad\qquad 2.29$$

$$\nabla \cdot B = 0 \qquad\qquad 2.30$$

$$\nabla \times H = J \qquad\qquad 2.31$$

The numerical solution of these equations is based on T-Ω formulation.
In this formulation, Ω is the nodal magnetic scalar potential, defined on the solution domain, while T is the edge-based electrical vector potential, which is only defined in the conducting region.

In the conducting region then

$$\nabla \times \frac{1}{\sigma}\nabla \times H + j\,\omega\,B = 0 \qquad\qquad 2.32$$

The magnetic field intensity can be expressed as

$$H = \nabla\Omega + T + H_p \qquad\qquad 2.33$$

where T is the electric vector potential due to the induced current, Ω is the magnetic scalar potential and H_p is the electric vector potential for source currents.

Substituting in the basic equations, we obtain the following formulation of the problem:

$$\nabla \cdot (\mu\nabla\Omega) = -\nabla \cdot \left(\mu H_p\right) \qquad\qquad 2.34$$

$$\nabla \times \frac{1}{\sigma}\nabla \times T + j\,\mu\,\omega(\nabla\Omega + T) = -\nabla \times \frac{1}{\sigma}\nabla \times H_p - j\mu\omega H_p \qquad\qquad 2.35$$

The main advantages of this formulation are:

- The use of edge elements for modelling source components avoid unphysical solutions
- In the nonconducting region only the scalar potential is calculated, increasing computing efficiency

An important point in T-Ω formulation is that the domain needs to be single-connected to allow using the scalar potential. To obtain this property, Ansys Maxwell automatically generate cut domains to allow handling multiple-connected domains.

2.5 Designs in Literature

2.5.1 Ball-joint type

Spherical actuator can realize multiple DOF motions in a single joint. Once there is current in stator coils, the PM poles in the rotor can be driven by the Lorentz force between them.

The rotation can be observed by energizing coils alternatively of just one layer. Similarly, for pitch and yaw, different longitudinal position current can be supplied to coils. Thus 3-DOF motions can be achieved by changing the order in which the current is supplied to the coils.

In the design of actuators, both the number of permanent magnets and the number and layout of coils are of great importance[10]. In Figure 8 and Figure 9 two layout are presented, one with two layers of equispaced coils and spherical tile-shaped permanent magnet poles[11], while the others presents three layers of coils and shell-shaped permanent magnet poles.
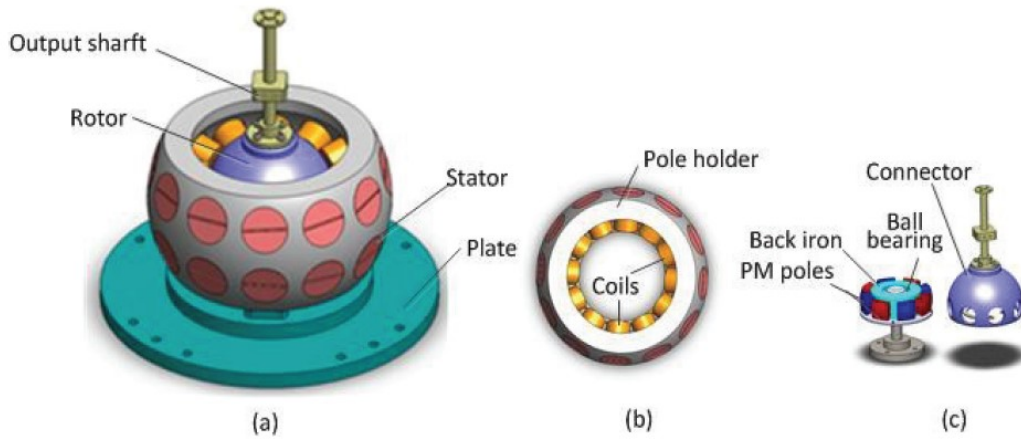
Figure 8 Actuator (a) stator with 2 layers of poles (b) rotor with spherical tile magnet (c)
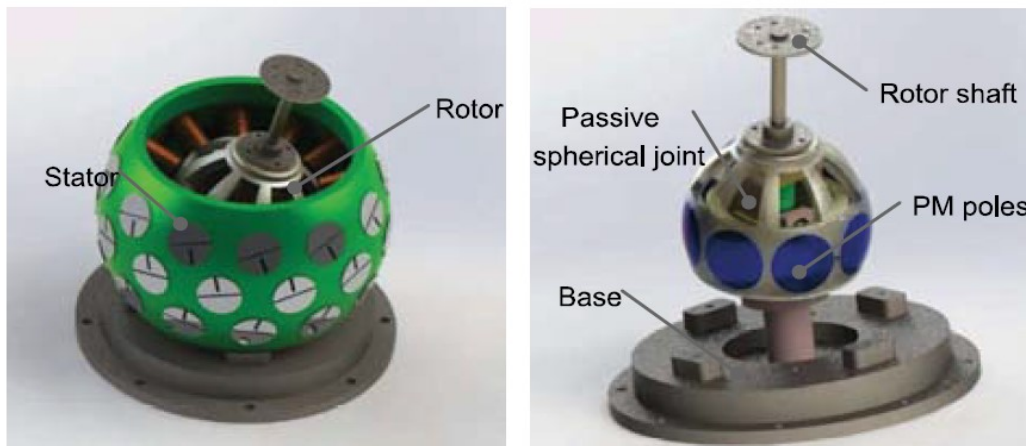
Figure 9 Actuator, stator with 3 layers of poles (left), rotor with conical magnet (right)

11

2.5.2   Deflection Type

This actuator is mainly constituted by stator and rotor spherical shells and an output shaft. The stator shell contains the magnet winding coils, while the rotor is made up of the magnets. Between the stator and the rotor there's a thin film of oil to reduce friction and adjust damping[12].
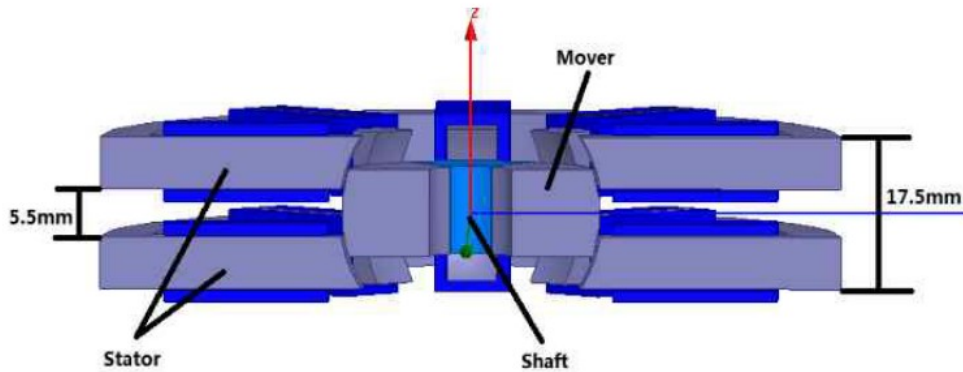
Figure 10 Actuator cross-section view

The motor works by leveraging the force generated between the magnetic field due to the coils and the permanent magnets [13]. The structure is shown in figure 4.
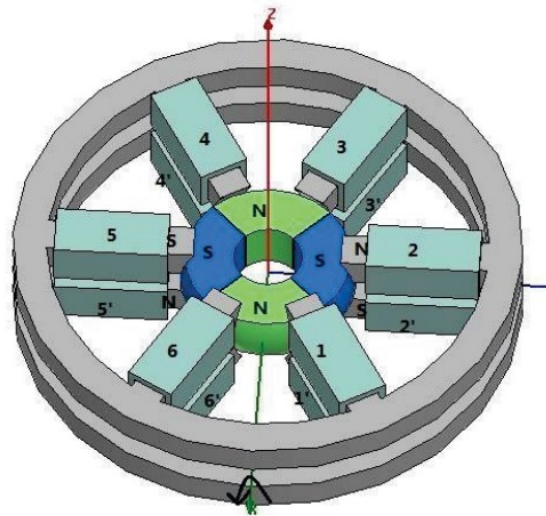
Figure 11 Actuator structure with rotor (inner) and stator (outer)

Energizing coils 2 and 5' will generate a N pole, while energizing coil 2' and 5 will produce an S pole. Pairs of poles with the same polarization generate mutually repulsive forces, while pairs with opposite polarization generate attractive forces, and the forces will in turn generate the torque that allows the motor to perform a movement. In the case in which coil 2, 5', 2' and 5 are energized, the resulting torque achieves a deflection about the X-axis [14].

To perform a deflection about the Y-axis, coils 3, 4, 1 and 6' need to be energized, generating an S pole, as well as energizing coils 3', 4', 1 and 6, generating N poles.

Finally, to achieve rotational movement about the Z-axis, the coils need to be energized in orders.

2.5.3 E-shaped stator and blade shaped rotor structure

The structure in the figure below has been presented in an effort to greatly reduce the weight of the rotor structure. This structure is similar to the impeller-shaped model and the common spherical-shaped case, in which the yoke and extra parts that have a lot of weight have been removed. The proportion between the stator poles to rotor poles is taken to be 6 to 8 [15].

The reason that the stator poles have been chosen to be less than the rotor poles is to increase wiring space in the stator. The magnet used is of the NdFeB type which has higher flux density amongst magnets available.
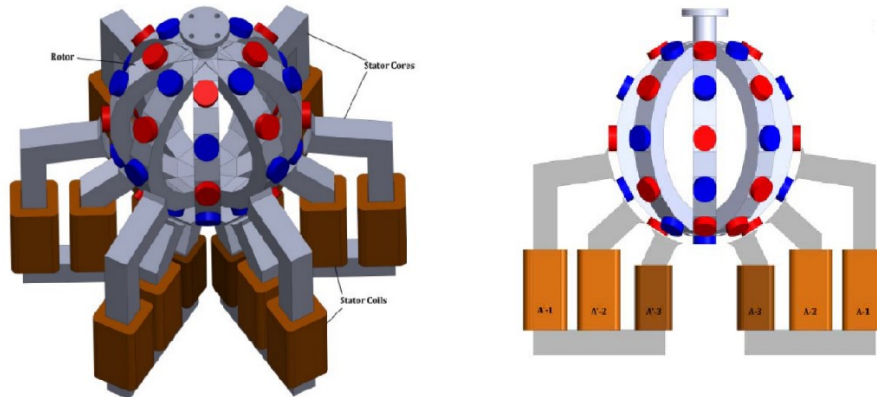
Figure 12 Actuator structure model

In the actuator structure presented, the coils are placed in the stator and this will widen the freedom of action of the system. In the stator, 6 E-shaped cores are placed. In order to be able to move in a certain direction in the simplest way, two of these cores must be excited at the same time[15].
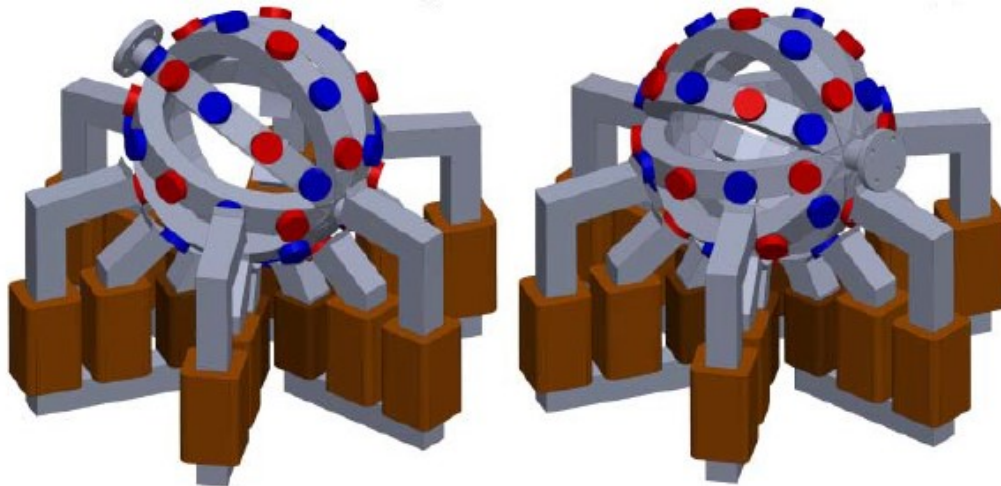
Figure 13 Actuator in rotated position

The figure above represents the rotation of the rotor thanks to the coils which are excited according to the flux applied in a certain moment relative to the x-axis and will provide the torque required to move to a certain direction. In order to set up the actuator in all directions, there will be at least a need for 6 different phases. The maximum amount of rotation for the rotor, due to the plates being dodecahedron (having 12 flat faces), will be between (-90, 90) degrees from the vertical.

2.5.4   Reaction Sphere

Attitude and orbit control systems (AOCSs) are some of the main satellite subsystems, as the orbital behaviour and pointing precision of stabilized satellites depends on them. Depending on the mission, AOCS of three-axis stabilized satellites normally require a minimum of three reaction wheels (RWs) or control moment gyroscopes (CMGs). The attitude of the satellite is changed by the reaction of the satellite main system to the torque generated by the wheels by the conservation of the total angular momentum [16]. A reaction sphere (RS) supported by magnetic bearings was proposed as an alternative to traditional momentum exchange devices.

As it can be accelerated in any direction, only a single device is needed to control all three axes of the satellite, without the disadvantage of friction due to mechanical joints [17].
The proposed device is a synchronous permanent magnet 3DoF motor. The PM and electromagnets are placed on the vertices of a regular polygon. The PM motor is made up of an 8-poles rotor and a stator composed by 20 air-core electromagnets, placed on the vertex of a dodecahedron. The Reaction Sphere proposed can be categorized as a three degree of freedom electromagnetic spherical actuator, and thanks to the spherical symmetry both of the magnetic and mechanical designs, it is isotropic, which means that its behaviour is the same independently of the axis of rotation considered, as its inertia matrix is diagonal with all diagonal terms equal [18].
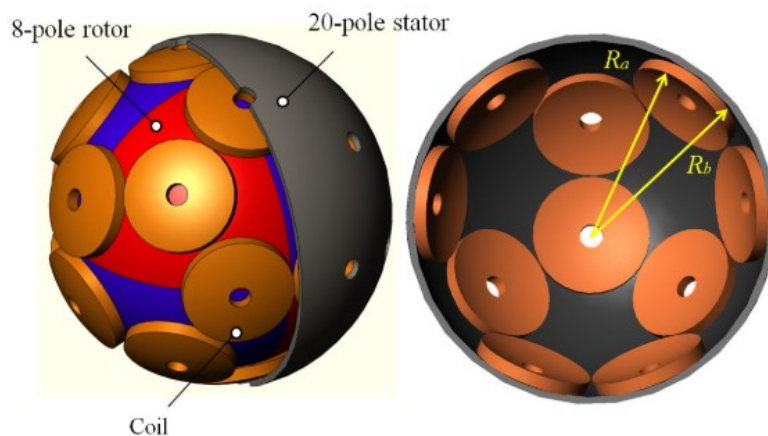
Figure 14 Schematic diagram of actuator (left) and stator (right)

The spherical rotor consists of eight bulk PM poles with truncated spherical shape adjusted on the back-iron structure with truncated octahedral shape. The 20 electromagnets that make up the stator are simultaneously employed to levitate the rotor inside the stator and to accelerate it to about any desired axis in order to produce the appropriate torque[19].
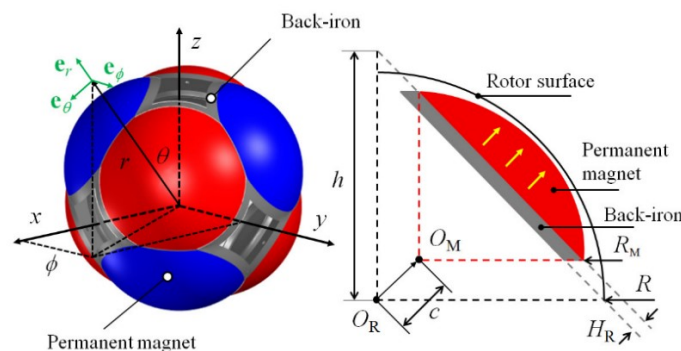
Figure 15 Rotor schematic drawing

14

3 DESIGNED CONFIGURATION

3.1 3D MODEL

The proposed design presents similarities with the deflection-type and reaction sphere type spherical actuators. The 3D model can be seen in the figure below.
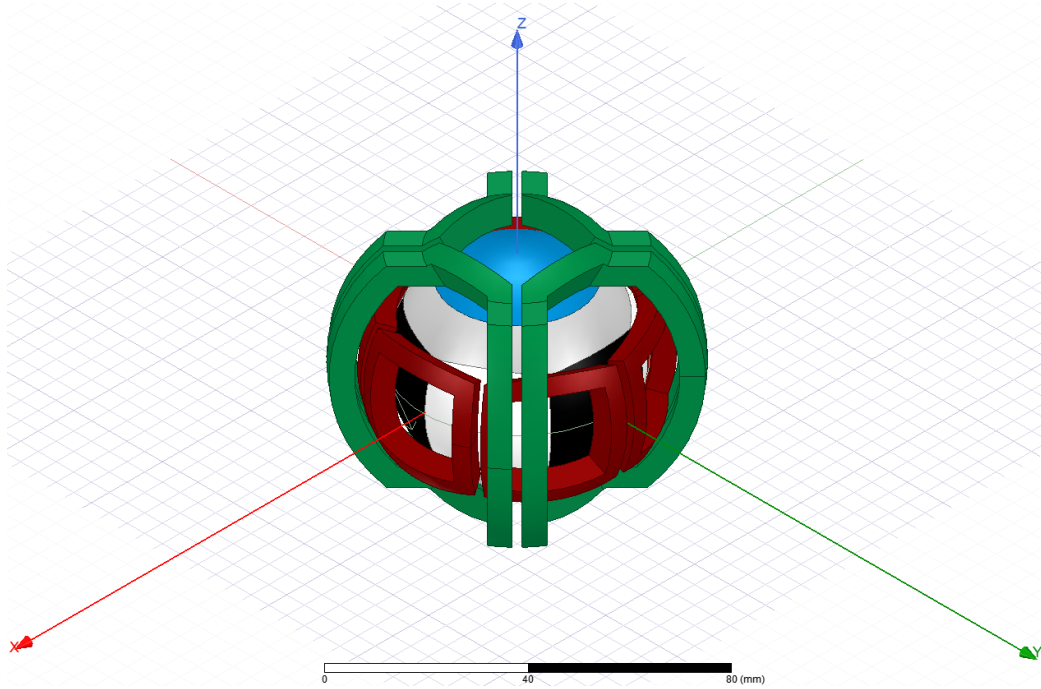
Figure 16 Proposed design 3D model

Table 1 present a summary of the main characteristics of the actuator.

R_i	R_o	R_{si}	R_{so}	α	β
[mm]	[mm]	[mm]	[mm]	[°]	[°]
20	26	32	38	60	60

Table 1 Geometrical properties

μ_r	σ	M	E
	[S/m]	[Am]	[GN/m^2]
1.045	625000	-838000	1470

Table 2 Main material properties of NdFe30

3.2 ROTOR

The rotor is spherical in shape. Six permanent magnets made of NdFe30 with alternating radial magnetization direction are placed around the equator of the rotor, while two permanent magnets made of NdFe30 with vertical magnetization direction are placed on the upper and lower hemisphere. The space between the radially magnetized magnets and the vertically magnetized ones is filled with aluminium.
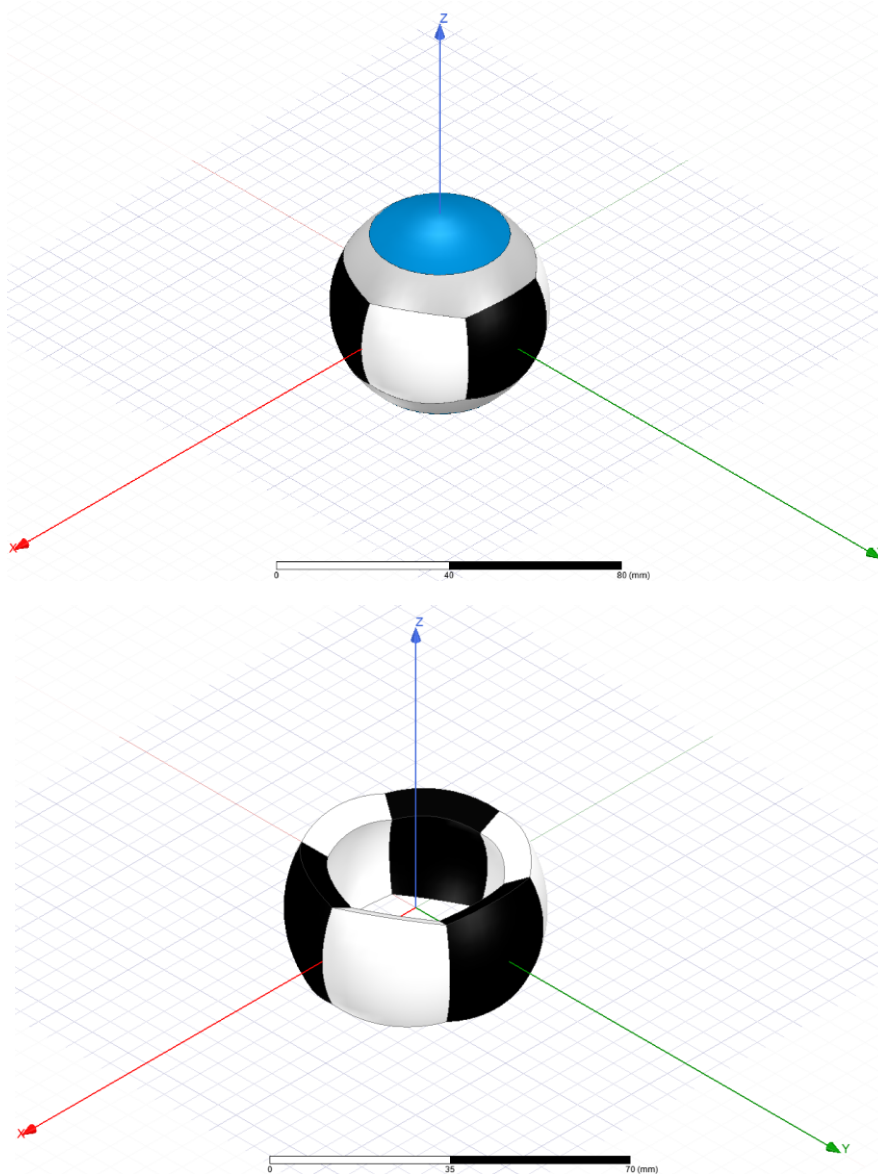
Figure 17 Rotor model (top) and spinning PM model (bottom)

The magnets have an inner radius R_b of 20mm, an outer radius R_r of 26mm, a horizontal angular aperture α of 60° and a vertical angular aperture β of 60°.

The main properties of NdFe30 are listed in Table 2.

3.3 STATOR

The stator is composed of a total of 10 coils, placed on 2 levels.
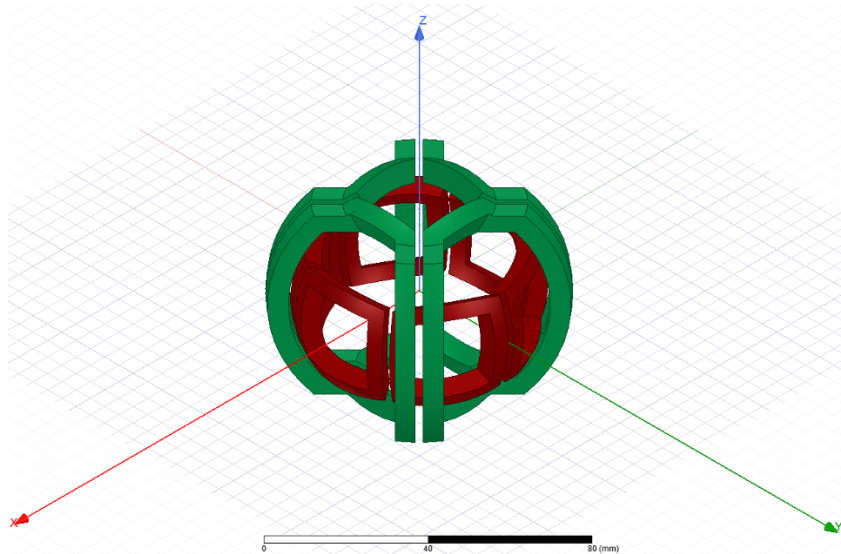
Figure 18 Complete stator coils model

The middle level is comprised of 6 coils, which envelope the equator of the rotor.

These coils are mainly responsible for the rotational movement around the z-axis.
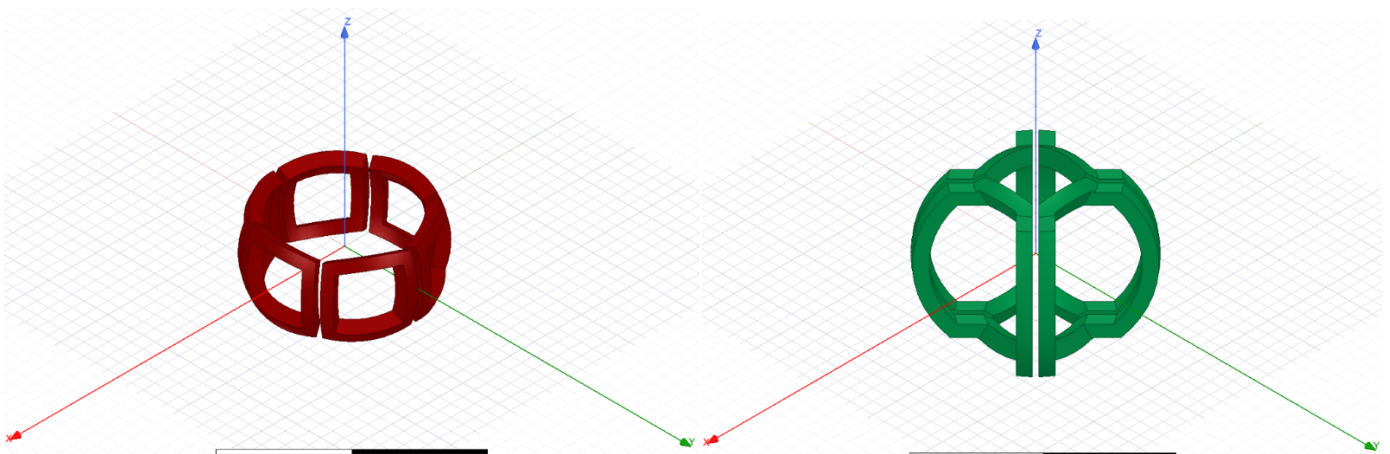
Figure 19 Spinning coils (left) and tilt coils (right)

The outer radius of this layer of coils is 31mm with an inner radius of 27mm.
The coils are shaped to follow the curvature of the rotor.

The second set of coils, comprised of 4 coils, envelopes the top and bottom of the sphere, enabling tilt motion. The coils are shaped to allow a 15° tilting rotation from the z-axis.

4 MAGNETIC FIELD MODELING

4.1 SPHERICAL HARMONICS MODEL

The magnetic field can be divided in 5 main regions:

- Air outside the rotor, region I
- Equatorial Permanent Magnet Pole, region II
- Hemispherical Permanent Magnet Pole, region III
- Ferromagnetic (iron) core, region IV
- Aluminium spacers, region V

In the case of PM regions, the flux density can be calculated as

$$B_i = \mu_0 \mu_i H_i + \mu_0 M_0 \qquad \qquad 4.1$$

While for the other regions it can be calculated as

$$B_i = \mu_0 \mu_i H_i \qquad \qquad 4.2$$

With i denoting the i-th region.

Considering the field H_i as irrotational, we can write

$$\nabla \times H_i = 0 \qquad \qquad 4.3$$

And referencing Helmholtz's Theorem, we can express the magnetic intensity as

$$H_i = -\nabla \Phi_i = -\left(\frac{\partial \Phi_i}{\partial x} + \frac{\partial \Phi_i}{\partial y} + \frac{\partial \Phi_i}{\partial z} \right) \qquad \qquad 4.4$$

And expressing the magnetic intensity in spherical coordinates gives

$$H_i = -\nabla \Phi_i = -\left(\frac{\partial \Phi_i}{\partial r} e_r + \frac{1}{r} \frac{\partial \Phi_i}{\partial \theta} + \frac{1}{r \sin \theta} \frac{\partial \Phi_i}{\partial \varphi} e_\varphi \right) \qquad \qquad 4.5$$

According to Maxwell Equation's, the magnetic field has the property of being solenoidal, i.e.

$$\nabla \cdot B_i = 0 \;\; \forall i \in \{I, II, III, IV, V\} \qquad \qquad 4.6$$

Substituting the equation shown above, and considering the symmetricity of the magnets in region II, we obtain Laplace's Equation for regions I, II, IV and V:

$$\nabla^2 \Phi_i = 0 \qquad \qquad 4.7$$

While for region III we obtain the Poisson's equation

$$\nabla^2 \Phi_{III} = \nabla \cdot \frac{M_0}{\mu_{III}} \qquad \qquad 4.8$$

The Laplace equation in spherical coordinates is

$$\frac{1}{r^2} \frac{\partial}{\partial r}(r^2 \, \Phi_i) + \frac{1}{r^2 \sin \theta} \frac{\partial}{\partial \theta}\left(\sin \theta \frac{\partial \Phi_i}{\partial \theta} \right) + \frac{1}{r^2 \sin^2 \theta} \frac{\partial \Phi_i}{\partial \phi} = 0 \qquad \qquad 4.9$$

Since the scalar potential Φ_i, using separation of variables, can be written as

$$\Phi_i(r, \theta, \phi) = R_i(r)\Theta_i(\theta)\Psi_i(\phi)$$

The general solution of the scalar potential can be expressed as [9]

$$\Phi_i = \sum_{n=0}^{\infty} \sum_{m=-n}^{n} \left(C_{ni}^m r^n + D_{ni}^m r^{-(n+1)} \right) \left(Y_n^m(\theta, \varphi) \right) \qquad 4.10$$

Where the function $Y_n^m(\theta, \phi)$ is the spherical harmonic function defined as

$$Y_n^m(\theta, \phi) = \sqrt{\frac{2n+1}{4\pi} \frac{(n-m)!}{(n+m)!}} \; P_n^m(\cos\theta) \, e^{i\,m\,\phi} = S_n^m \, P_n^m(\cos\theta) e^{i\,m\,\phi} \qquad 4.11$$

With $P_n^m(\cos\theta)$ associated Legendre function.

4.1.1 Spherical Expansion of M_{0r}

Letting M_0 as the magnitude of the residual magnetization vector $\boldsymbol{M_0}$, the radial component is [20]

$$M_{0r} = (-1)^{p-1} M_0 \cos\left[\phi - \alpha_0 - \frac{2\pi}{P}(p-1) \right] \sin\theta \qquad 4.12$$

The radial component of the magnetization vector can be approximated using spherical harmonics[9]

$$M_r(\theta, \phi) = \sum_{n}^{\infty} \sum_{k}^{n} C_{nm} Y_n^m(\theta, \varphi) \qquad 4.13$$

Where the spherical harmonic coefficients can be obtained by

$$C_{nm} = \int_0^{2\pi} \int_0^{\pi} M_{0r}(\theta, \varphi) Y_n^{m*}(\theta, \varphi) \sin\theta \; d\theta d\varphi \qquad 4.14$$

Where Y_n^{m*} is the complex conjugate of the spherical harmonic Y_n^m.

By reordering the integral we get to

$$C_{nm} = \int_0^{2\pi} f(\varphi) e^{-i\,m\,\varphi} d\varphi \int_0^{\pi} S_n^m \, P_n^m(\cos\theta) \sin^2\theta \; d\theta \qquad 4.15$$

By imposing boundary conditions, expressions for C and D parameters can be derived, with $C \equiv 0$ and $D = C_{nm} d_n$, so

$$\varphi(r, \theta, \varphi) = \sum_{n}^{\infty} \sum_{m=-n}^{n} C_{nm} d_n r^{-n-1} \, Y_n^m(\theta, \varphi) \qquad 4.16$$

And finally

$$B_{1r} = -\mu_0 \frac{\partial\varphi}{\partial r} = -\mu_0 \sum_{n}^{\infty} \sum_{m=-n}^{n} (-n-1) \cdot C_{nm} d_n r^{-n-2} \, Y_n^m(\theta, \varphi) \qquad 4.17$$

The rotor design being investigated presents 6 poles (P=6) and the center line angle α_0 is $\frac{\alpha}{2} + \alpha \cdot (p-1)$ where $\alpha = 60°$

Given the definitions of spherical harmonics and associated Legendre functions [8]

$$Y_n^m(\theta, \varphi) = \sqrt{\frac{2n+1}{4\pi} \frac{(n-|m|)!}{(n+|m|)!}} \; P_n^{|m|}(\cos\theta) e^{i\,m\varphi} \qquad 4.18$$

$$Y_n^{m*}(\theta, \varphi) = (-1)^m Y_n^{-m}(\theta, \varphi)$$ 4.19

$$Y_n^{m*}(\theta, \varphi) = (-1)^m \sqrt{\frac{2n+1}{4\pi} \frac{(n-|m|)!}{(n+|m|)!}} \, P_n^{|m|}(\cos\theta) e^{-i\,m\varphi}$$ 4.20

$$P_n^m(x) = \frac{(-1)^m}{2^n n!} (1-x^2)^{\frac{m}{2}} \frac{d^m}{dx^{n+m}} (x^2-1)^n$$ 4.21

Substituting into 1.2 we get:

$$C_{nm} = (-1)^m M_0 \sqrt{\frac{2n+1}{4\pi} \frac{(n-|m|)!}{(n+|m|)!}} \cdot \int_0^{2\pi} (-1)^{p-1} \cos\left(\varphi - \alpha_0 - \frac{2\pi(p-1)}{P}\right) e^{-i\,m\varphi} d\varphi$$
$$\cdot \int_0^\pi P_n^{|m|}(\cos\theta) \sin^2\theta \, d\theta$$ 4.22

Which we can transform to

$$C_{nm} = (-1)^m M_0 (a \pm ib) \frac{c}{\sqrt{\pi}}$$ 4.23

By setting

$$a \pm ib = \int_0^{2\pi} (-1)^{p-1} \cos\left(\varphi - \alpha_0 - \frac{2\pi(p-1)}{P}\right) e^{-i\,m\varphi} d\varphi$$ 4.24

$$\frac{c}{\sqrt{\pi}} = \int_0^\pi \sqrt{\frac{2n+1}{4\pi} \frac{(n-|m|)!}{(n+|m|)!}} \, P_n^{|m|}(\cos\theta) \sin^2\theta \, d\theta$$ 4.25

Considering the case in which $m = \pm3, n = 3, P = 6$ we get:

$$P_3^3(\cos\theta) = -15(1 - \cos^2\theta)^{\frac{3}{2}}$$ 4.26

$$P_3^{-3}(\cos\theta) = \frac{1}{48} (1 - \cos^2\theta)^{\frac{3}{2}}$$ 4.27

$$a \pm ib = \int_0^{2\pi} (-1)^{p-1} \cos\left(\varphi - \alpha_0 - \frac{\pi(p-1)}{3}\right) e^{-i\,(\pm3)\,\varphi} d\varphi$$ 4.28

$$\frac{c}{\sqrt{\pi}} = \int_0^\pi \sqrt{\frac{7}{4\pi} \frac{(3\mp3)!}{(3\pm3)!}} \, P_3^{\pm3}(\cos\theta) \sin^2\theta \, d\theta$$ 4.29

with $p \in \{1..6\} \subset \mathbb{Z}$, φ restricted to $\frac{\pi}{3}(p-1) + \alpha_0 - \frac{\alpha}{2} \le \varphi \le \frac{\pi}{3}(p-1) + \alpha_0 + \frac{\alpha}{2}$ and θ restricted to $\frac{\pi}{2} - \frac{\beta}{2} \le \theta \le \frac{\pi}{2} + \frac{\beta}{2}$.

So

$$C_{3,3} = -M_0 \frac{a + ib}{\sqrt{\pi}} c \qquad 4.30$$

$$C_{3,-3} = -M_0 \frac{a - ib}{\sqrt{\pi}} c \qquad 4.31$$

And considering that setting $m = \pm 3, n = 3$ and $\theta \in \mathbb{R}^+$ the spherical harmonics have the following expression [1]

$$Y_3^{-3} = \frac{1}{8} \cdot \sqrt{\frac{35}{\pi}} \cdot e^{-i3\phi} \cdot \sin(\theta)^3 \qquad 4.32$$

$$Y_3^3 = -\frac{1}{8} \cdot \sqrt{\frac{35}{\pi}} \cdot e^{i3\phi} \cdot \sin(\theta)^3 \qquad 4.33$$

Applying the boundary conditions we get that

$$d_n = \frac{-d_n^\top}{d_n^\perp} \qquad 4.34$$

$$d_n^\top = R_r^{n+2} + \frac{\mu_m(2n+1)R_b^{n+2}R_r^{2n+1}}{(\mu_r - \mu_m)nR_b^{2n+1} - |\mu_r n + \mu_m(n+1)|R_r^{2n+1}} \qquad 4.35$$

$$d_n^\perp = (\mu_m - 1)(n+1) + \frac{\mu_m(2n+1)|\mu_r n + \mu_m(n+1)|R_r^{2n+1}}{(\mu_r - \mu_m)nR_b^{2n+1} - |\mu_r n + \mu_m(n+1)|R_r^{2n+1}} \qquad 4.36$$

Considering only the first harmonic we have

$$\Phi_I = \xi_3^{-3} r^{-4} Y_3^{-3} + \xi_3^3 r^{-4} Y_3^3 \qquad 4.37$$

Where

$$\xi_3^{-3} = C_{3,-3} d_3 = -M_0 \frac{d_3}{\sqrt{\pi}} (a - bi)c \qquad 4.38$$

$$\xi_3^3 = C_{3,3} d_3 = -M_0 \frac{d_3}{\sqrt{\pi}} (a + bi)c \qquad 4.39$$

And substituting

$$\Phi_I = -r^{-4} M_0 \frac{d_3}{\sqrt{\pi}} (a - ib)c \cdot \frac{1}{8} \cdot \sqrt{\frac{35}{\pi}} \cdot e^{-i\,3\varphi} \cdot \sin^3(\theta)$$

$$+ r^{-4} M_0 \frac{d_3}{\sqrt{\pi}} (a + bi)c \cdot \frac{1}{8} \cdot \sqrt{\frac{35}{\pi}} \cdot e^{i\,3\varphi} \cdot \sin^3(\theta) \qquad 4.40$$

$$\Phi_I = r^{-4} \frac{M_0 d_3}{\sqrt{\pi}} c \frac{1}{8} \sqrt{\frac{35}{\pi}} \sin^3 \theta \left[-(a - ib) \cdot e^{-3i\varphi} + (a + ib) \cdot e^{3i\varphi} \right] \qquad 4.41$$

$$\Phi_I = r^{-4} \frac{M_0 d_3}{\pi} c \frac{1}{8} \sqrt{35} \sin^3 \theta \cdot 2\, i\, [a \sin(3\varphi) + b \cos(3\varphi)] \qquad 4.42$$

$$\Phi_I = r^{-4} \frac{M_0 d_3}{\pi} c \frac{1}{4} \sqrt{35} \sin^3 \theta \cdot i[a \sin(3\varphi) + b \cos(3\varphi)] \qquad 4.43$$

Now, since

$$B_I = \mu_0 H_I = -\mu_0 \nabla \Phi_I \qquad\qquad 4.44$$

in spherical coordinates we have:

$$B_I = -\mu_0 \cdot \left(\frac{\partial \Phi_I}{\partial r} \, \hat{r} + \frac{1}{r} \frac{\partial \Phi_I}{\partial \theta} \, \hat{\theta} + \frac{1}{r \sin\theta} \frac{\partial \Phi_I}{\partial \varphi} \, \hat{\varphi} \right) \qquad\qquad 4.45$$

$$B_r = \mu_0 r^{-5} \frac{M_0 d_3}{\pi} \, c \, \sqrt{35} \, \sin^3 \theta \, i \, [a \sin(3\varphi) + b \cos(3\varphi)] \qquad\qquad 4.46$$

$$B_\theta = -\mu_0 r^{-5} \frac{M_0 d_3}{\pi} \, c \frac{3}{4} \, \sqrt{35} \, \sin^2 \theta \cos\theta \, i \, [a \sin(3\varphi) + b \cos(3\varphi)] \qquad\qquad 4.47$$

$$B_\varphi = -\mu_0 r^{-5} \frac{M_0 d_3}{\pi} \, c \frac{3}{4} \, \sqrt{35} \, \sin^2 \theta \, i [a \cos(3\varphi) - b \sin(3\varphi)] \qquad\qquad 4.48$$
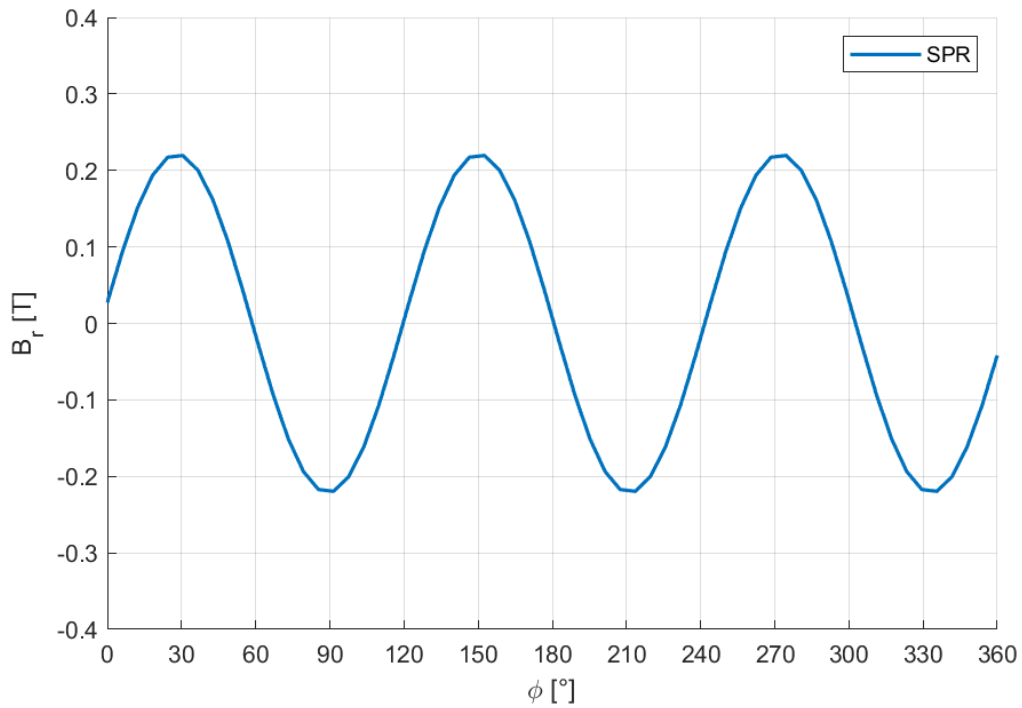
Figure 20 B_r by spherical harmonic considering only the first harmonic

4.2 MAGNETIC EQUIVALENT CHARGE MODEL

In the magnetic equivalent charge model, a permanent magnet is reduced to an equivalent distribution of magnetic "charges" on the surfaces of the magnet, and these charges are then used as sources in the magnetostatics field equation.

For current-free regions, we have that

$$\nabla \times H = 0 \qquad\qquad 4.49$$
$$\nabla \cdot B = 0 \qquad\qquad 4.50$$

In spherical coordinates, we can say that the magnetization vector is

$$M = -M_0 \,\hat{\rho} \qquad\qquad 4.51$$

The scalar potential can be written as [7]

$$\phi_m(r) = \frac{1}{4\pi} \int_V \frac{\rho_m}{|r - r'|} dv + \frac{1}{4\pi} \int_s \frac{\sigma_m}{|r - r'|} ds \qquad\qquad 4.52$$

$$\rho_m = -\nabla' \cdot M \qquad\qquad 4.53$$

$$\sigma_m = M \cdot n \qquad\qquad 4.54$$

$$B(r) = \mu_0(-\nabla\phi_m) \qquad\qquad 4.55$$

$$B(r) = -\mu_0 \nabla \left[\frac{1}{4\pi} \int_V \frac{\rho_m}{|r - r'|} dv + \frac{1}{4\pi} \int_s \frac{\sigma_m}{|r - r'|} ds \right]$$
$$= -\frac{\mu_0}{4\pi} \int_V \rho_m \nabla \frac{1}{|r - r'|} dv - \frac{\mu_0}{4\pi} \int_s M \cdot n \, \nabla \frac{1}{|r - r'|} ds \qquad\qquad 4.56$$

with

$$\nabla \frac{1}{|r - r'|} = -\frac{1}{2} \frac{1}{a^{\frac{3}{2}}} \left[\frac{\partial a}{\partial \rho} \hat{e}_\rho + \frac{1}{\rho} \frac{\partial a}{\partial \theta} \hat{e}_\theta + \frac{1}{\rho \sin\theta} \frac{\partial a}{\partial \varphi} \hat{e}_\varphi \right] \qquad\qquad 4.57$$

where

$$a = \rho^2 + \rho'^2 - 2\rho\rho'[\sin\theta \sin\theta' \cos(\varphi - \varphi') + \cos\theta \cos\theta'] \qquad\qquad 4.58$$

And substituting we obtain:

$$\nabla \frac{1}{|r - r'|} = -\frac{1}{a^{\frac{3}{2}}} \begin{cases} \left(\rho - \rho'(\sin\theta \sin\theta' \cos(\varphi - \varphi') + \cos\theta \cos\theta')\hat{e}_\rho \right. \\ -\rho'(\cos\theta \sin\theta' \cos(\varphi - \varphi') - \sin\theta \cos\theta')\hat{e}_\theta \\ \left. \rho'(\sin\theta \sin\theta' \sin(\varphi - \varphi'))\hat{e}_\varphi \right. \end{cases} \qquad\qquad 4.59$$

The surface normals in spherical coordinates are expressed by θ, φ since the surface is also spherical.

If we call α, β, Θ respectively the angular width, angular height, offset angle along θ, the normals of the six faces of a tile become:

$$n_1 = \sin\varphi \cos\theta \, \hat{e}_x + \sin\varphi \sin\theta \, \hat{e}_x + \cos\varphi \, \hat{e}_z = -n_3$$
$$n_2 = -\sin\frac{\phi_0}{2} \hat{e}_x + \cos\frac{\phi_0}{2} \hat{e}_z$$

$$n_4 = -\sin\frac{\phi_0}{2}\hat{e}_x + \cos\frac{\phi_0}{2}\hat{e}_z$$
$$n_5 = -\sin\theta_1\,\hat{e}_x + \cos\theta_1\,\hat{e}_y$$
$$n_6 = \sin\theta_2\,\hat{e}_x - \cos\theta_2\,\hat{e}_y$$

And the infinitesimal surface element dS for the integrals are

$$dS_1 = \rho_0^2\sin\varphi\,d\theta d\varphi$$
$$dS_3 = \rho_i^2\sin\varphi\,d\theta d\varphi$$
$$dS_{2,4} = \rho d\rho d\theta$$
$$dS_{5,6} = \rho\sin\theta\,d\rho d\varphi$$

We have that

$$n_1 = \hat{\rho}$$

$$M = M_0\hat{\rho}$$

Which give the following expressions for magnetic surface charge densities:

$$\sigma_{m_1} = -\sigma_{m_2} = M_0$$

Considering only surfaces 1 and 2, where the radii are ρ_1 and ρ_2 respectively, we get that the radial component of the magnetic flux density can be calculated as[21]:

$$B_r(r,\theta,\varphi) = -\frac{\mu_0 M_0}{2\pi}\iiint \frac{\rho'\sin(\theta')\,[\rho - \rho'(\sin\theta\sin\theta'\cos(\varphi-\varphi') + \cos\theta\cos\theta')]}{\left(\rho^2 + \rho'^2 - 2\rho\rho'[\sin(\theta)\sin(\theta')\cos(\varphi-\varphi') + \cos(\theta)\cos(\theta')]\,\right)^{\frac{3}{2}}}d\rho'd\varphi'd\theta' +$$

$$+\frac{\mu_0 M_0}{4\pi}\iint \frac{\rho_2^2\sin(\theta')\,[\rho - \rho_2(\sin\theta\sin\theta'\cos(\varphi-\varphi') + \cos\theta\cos\theta')]}{(\rho^2 + \rho_2^2 - 2\rho\rho_2[\sin(\theta)\sin(\theta')\cos(\varphi-\varphi') + \cos(\theta)\cos(\theta')]\,)^{\frac{3}{2}}}d\varphi'd\theta' +$$

$$-\frac{\mu_0 M_0}{4\pi}\iint \frac{\rho_1^2\sin(\theta')\,[\rho - \rho_1(\sin\theta\sin\theta'\cos(\varphi-\varphi') + \cos\theta\cos\theta')]}{(\rho^2 + \rho_1^2 - 2\rho\rho_1[\sin(\theta)\sin(\theta')\cos(\varphi-\varphi') + \cos(\theta)\cos(\theta')]\,)^{\frac{3}{2}}}d\varphi'd\theta' \qquad 4.60$$
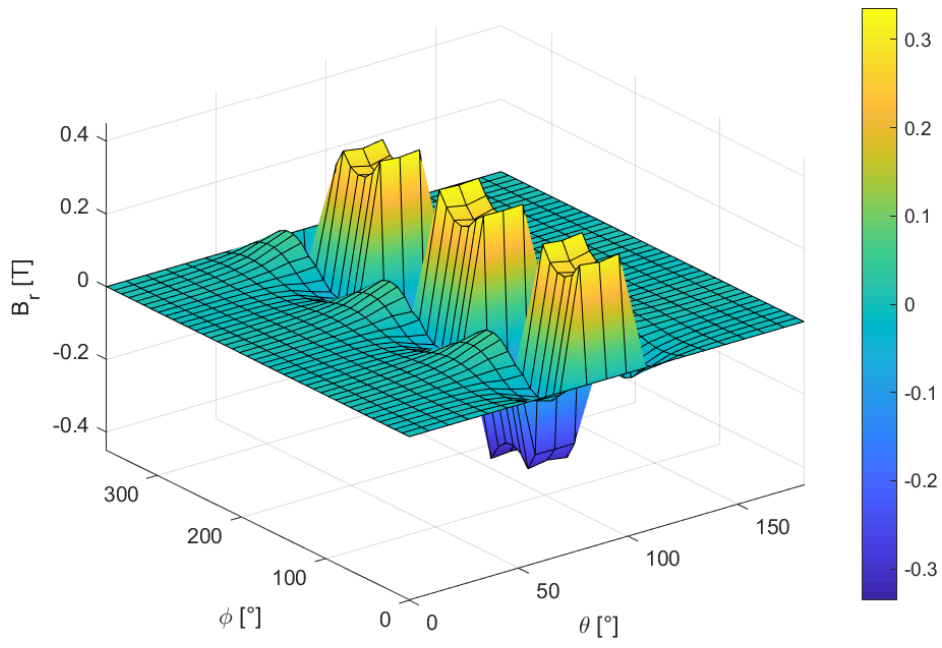
Figure 21 Surface plot of B_r
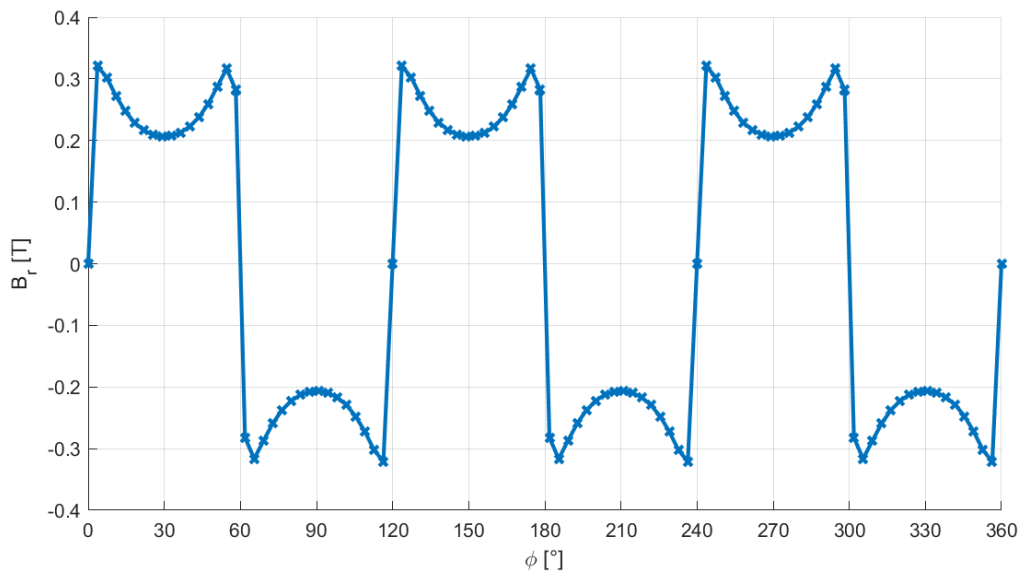
Figure 22 B_r at θ = 90°

4.3 FINITE ELEMENT MODEL

A finite element model is developed using the software Ansys Maxwell[22], which uses FEM to perform the magnetostatics analysis. Numerical solution of such equations is based on T-Ω formulation in which Ω is nodal-based magnetic scalar potential, defined in the entire solution domain, and T is edge-based electrical vector potential, defined only in the conducting eddy-current region

4.3.1 B_r on plane XY

As can be seen in the graph below, the magnetic flux density along the equator, at a distance 0.5mm from the rotor, varies between 0.3T and -0.30T. Notice the significant discontinuities at the boundary between different permanent magnets.
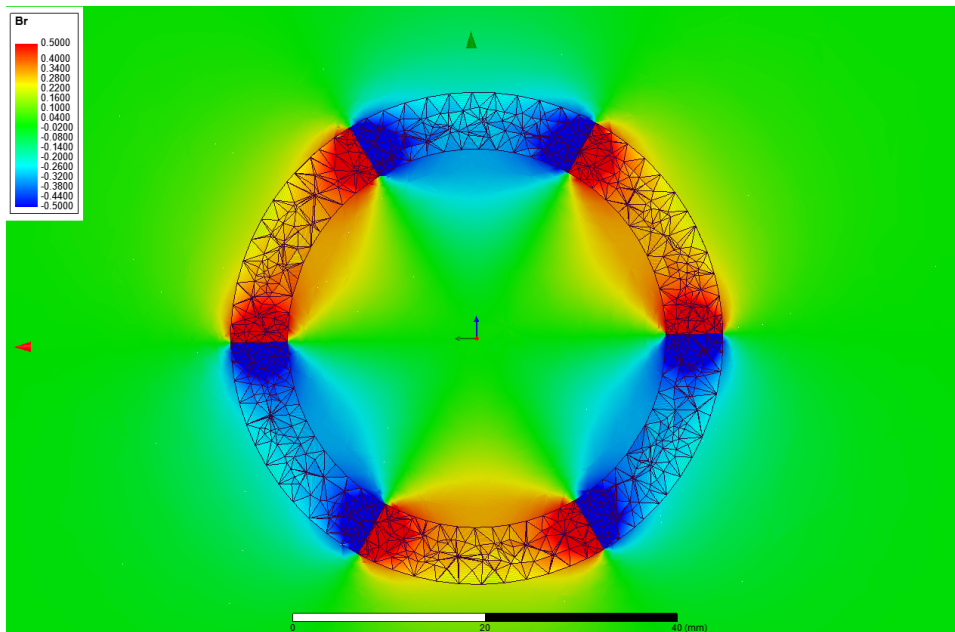
Figure 23 Plot of B_r on the XY plane
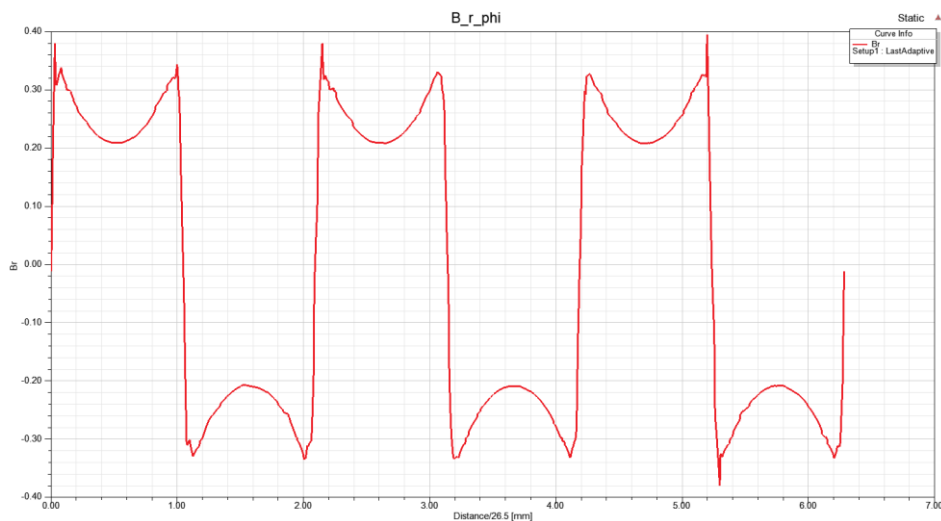
Figure 24 Plot of B_r on the XY plane at r=26.5mm and \theta=90°

4.3.2 B_r on plane YZ

As can be seen in the graph below, the magnetic flux density along the meridian, at a distance 0.5mm from the rotor, varies between 0.30T and -0.30T. Notice the effect of the equatorial permanent magnet and that of the top and bottom magnet.
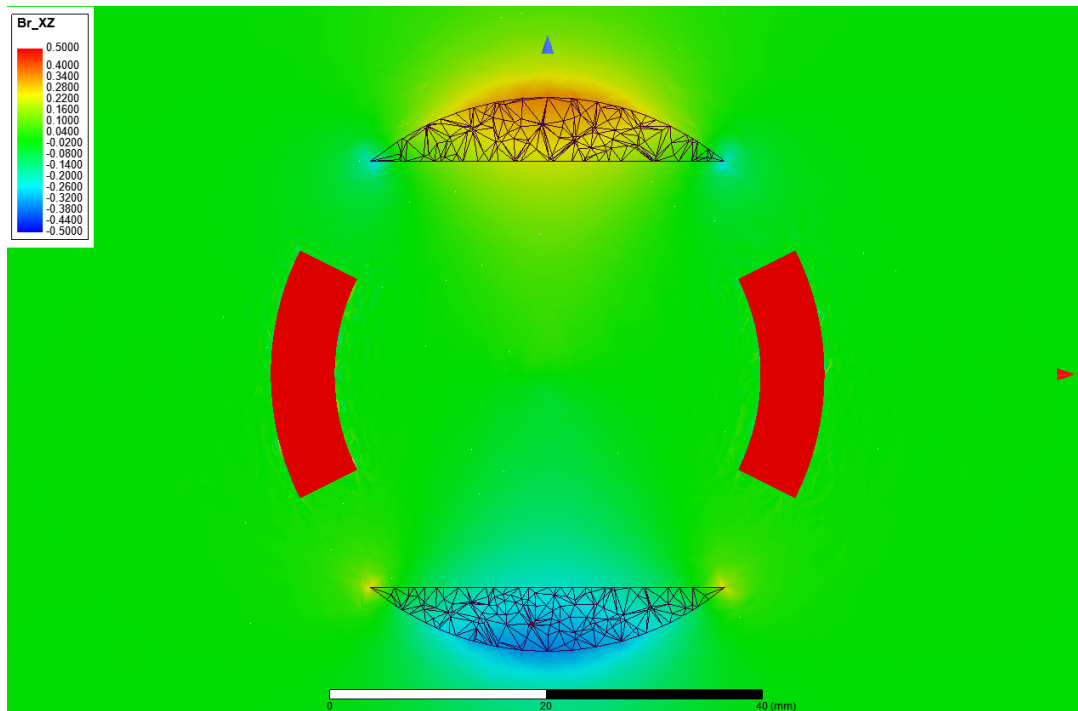
Figure 25 Plot of B_r on the XZ plane
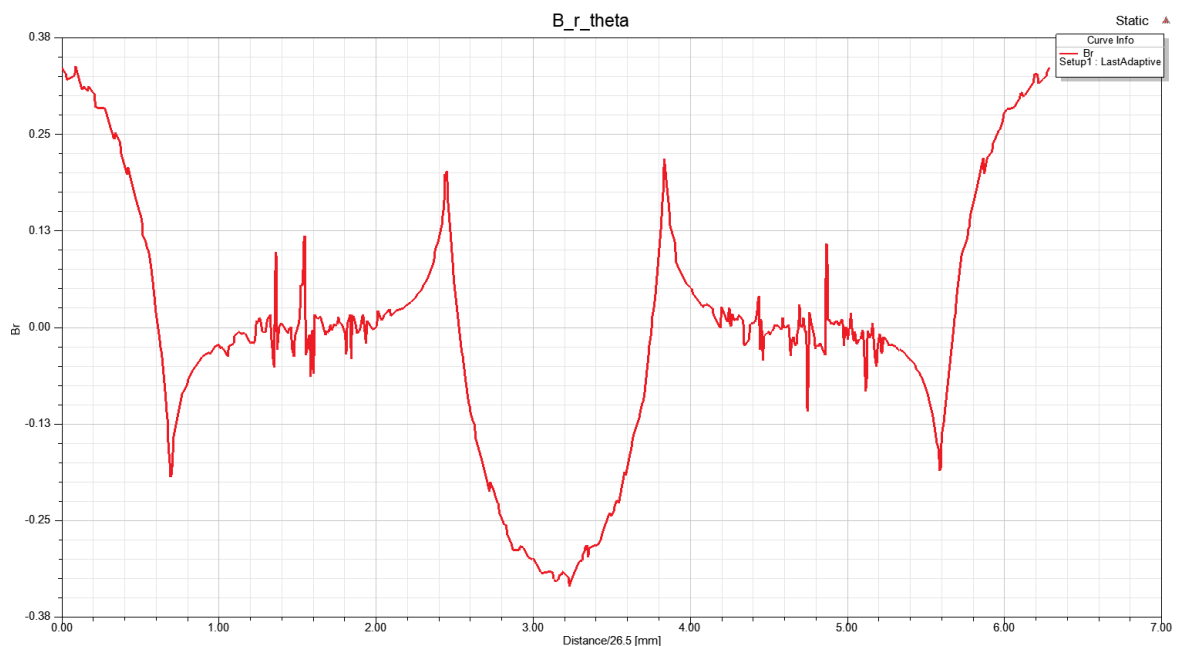
Figure 26 Plot of B_r on the XZ plane at r=26.5mm and \phi=0°

4.4 COMPARISON OF B_r

The following graph summarizes the result from the two analytical model as well as comparing them with the FEM model.
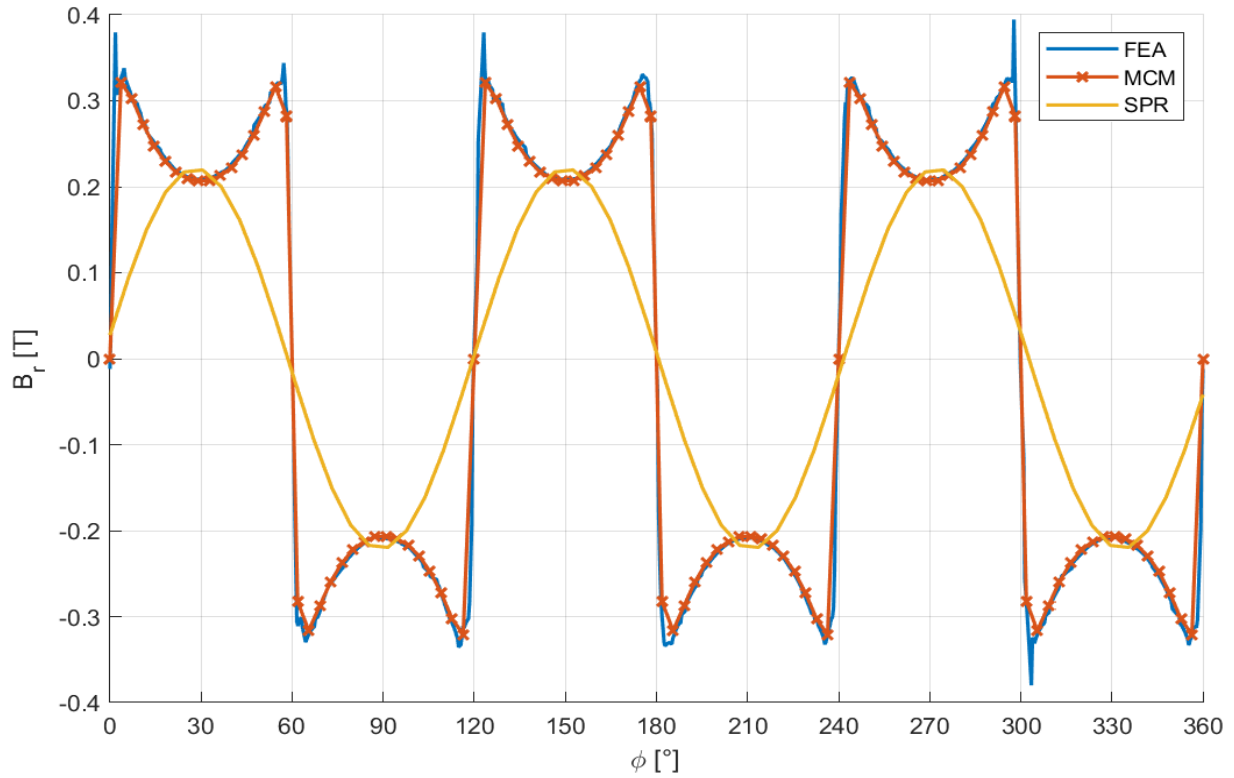
Figure 27 Comparison of finite element, magnetic charge and spherical harmonics models

Notice how the spherical harmonic result are quite far from the other two models. This is mainly due to the fact that only the main spherical harmonic was considered. To improve the results, it's possible, although more computationally expensive, to take into account higher order spherical harmonics.

5 TORQUE MODELLING

5.1 LORENTZ TORQUE

Lorentz force is commonly defined as the combination of electric and magnetic force on a point charge due to electromagnetic fields, so considering a single charge q moving with speed v we have:

$$F = q\,E + q\,v \times B$$

For a continuous charge distribution, the equation becomes

$$dF = dq\,(E + v \times B)$$

Or dividing by the volume dV:

$$f = \rho(E + v \times B)$$

And since the we can write the current density as $J = \rho\,v$ we obtain the volume integral

$$F = \int_V (\rho E + J \times B)dV$$

And by using the definition of electric current I and considering a stationary wire, we can write

$$F = I \int_V d\ell \times B$$

The torque can be written as the cross product of the moment arm r and the force dF so

$$dT_i = r \times Id\ell \times B_r$$

And the torque generated by the i-th coil is then[19]

$$T_i = I \int_V r \times d\ell \times B_r dV$$

5.2 VIRTUAL TORQUE

To compute the torque on an object, Ansys Maxwell uses the principle of virtual work. In general, this can be expressed as

$$T_B = \frac{dW(\theta, i)}{d\theta}\bigg|_{i=const}$$

where W is the magnetic coenergy of the system defined as

$$W = \frac{1}{2} \int_V B \cdot H\,dV \ \text{ for linear material}$$

$$W = \int_V w_c \cdot dV = \int_V \left(\int_0^H B \cdot dH \right) dV \ \text{ for nonlinear materials}$$

Unlike the classical virtual work method, the object is not actually rotated during the force computation, and only the outside tetrahedra are virtually distorted, without need to solve the system again. This way, the change in coenergy is given by the change in the coenergy of these tetrahedra[23].

5.3 SPINNING TORQUE
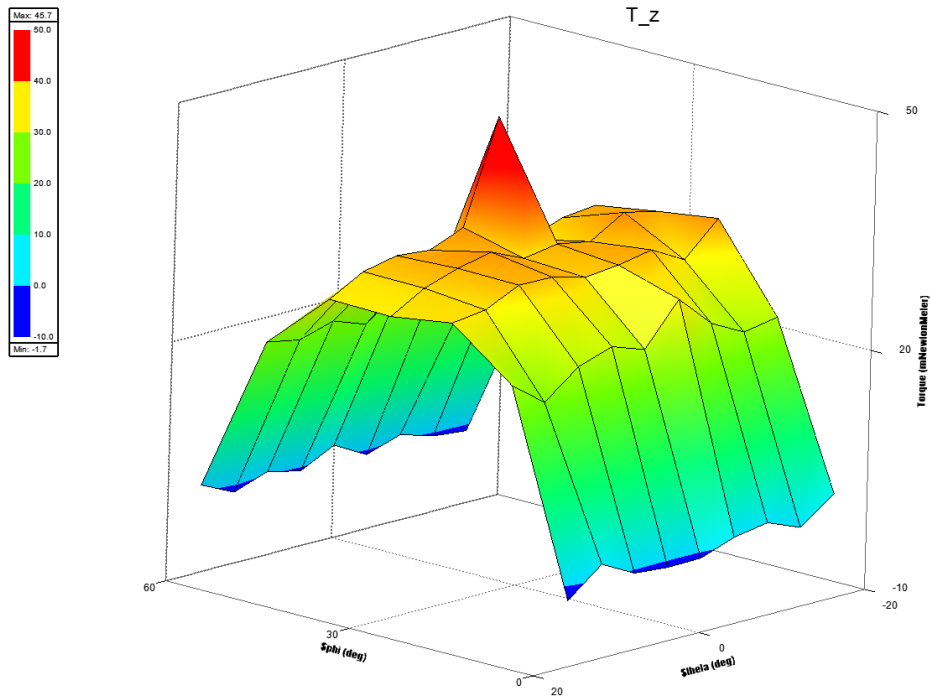
Figure 28 T_z in the range ϕ 0-60° θ -16-+16

In Figure 7 the spinning torque due to the excitation of a single coil is shown.
Note how the spinning torque increases with the rotational angle up until it reaches 30° and then starts to decrease.
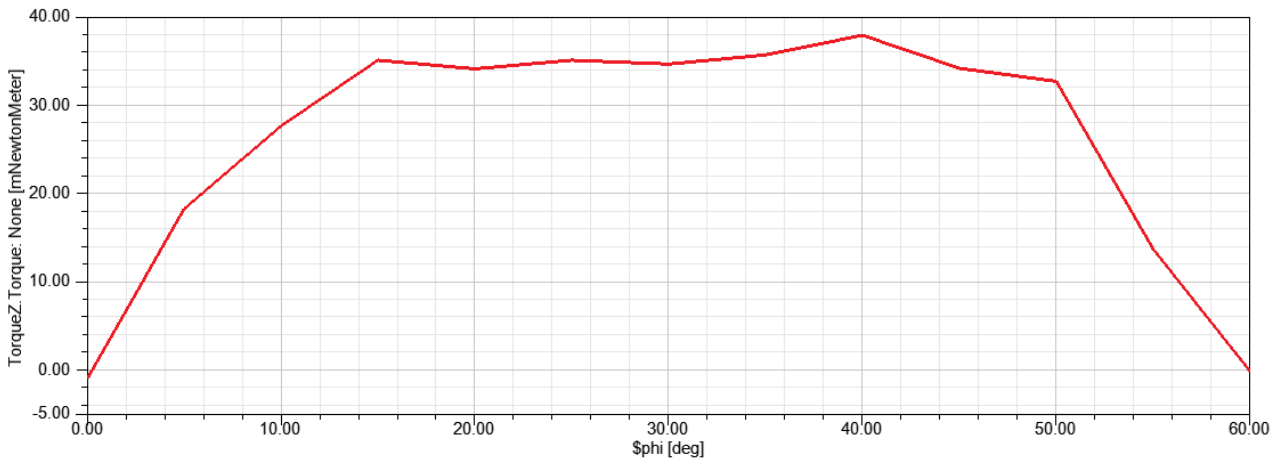
Figure 29 T_z at various rotated positions around the z-axis

From Figure 8 it can be clearly seen that spinning torque has a linear relationship with the current applied to the coil.
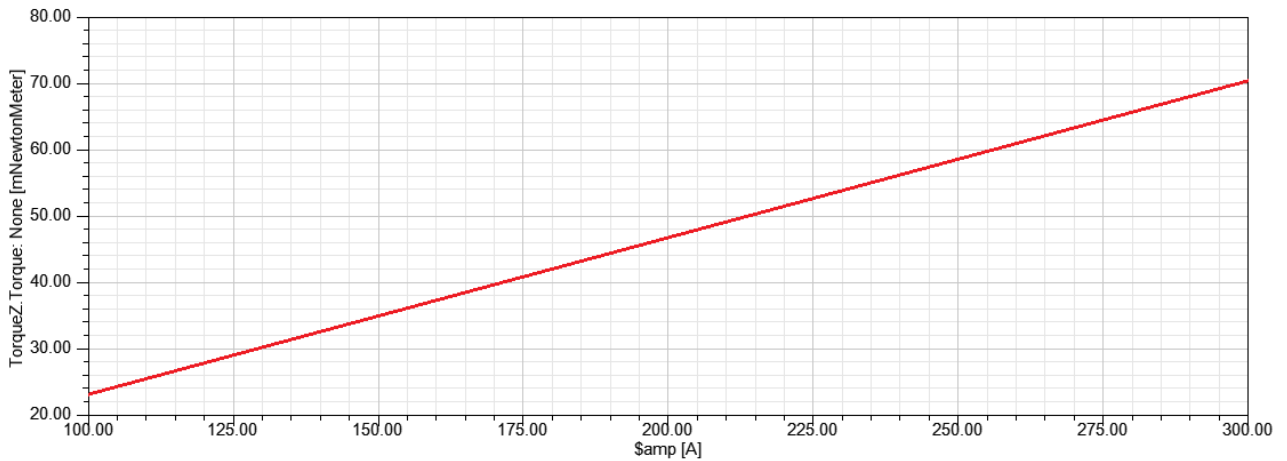
Figure 30 Change in spinning torque with changes in the applied current

Figure 9 shows the spinning torque obtained when the rotor is in a tilted position. It can be seen that the spinning torque has only a slight decrease when the rotor is tilted. By looking at the Torque surface in Figure 10, we can see that this holds true for most of the tilting range, even if the surface is somewhat rough due to the low number of points caused by the very long computational time require by the FEM analysis.
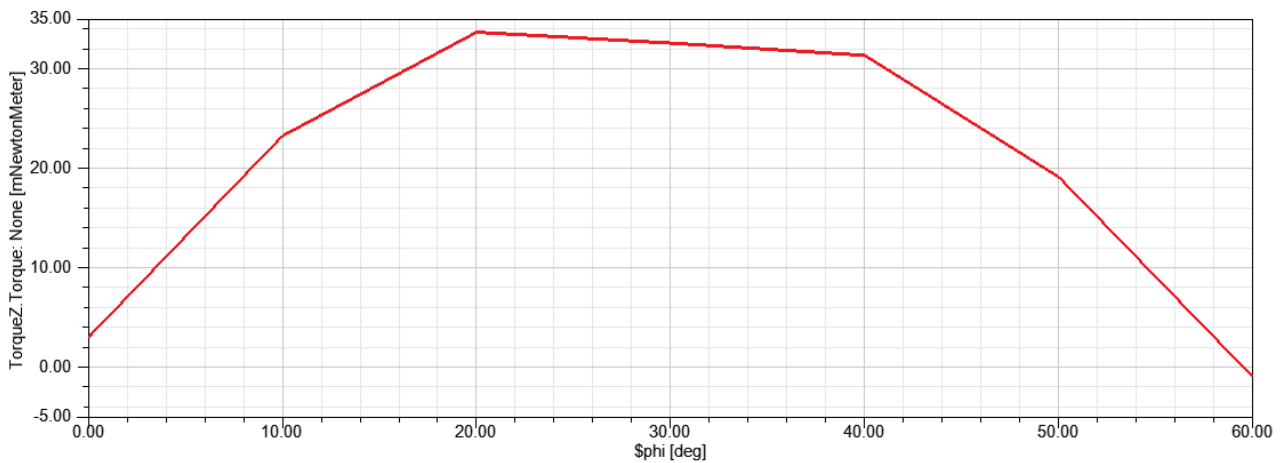
Figure 31 T_z in tilted position ($theta = 12°)
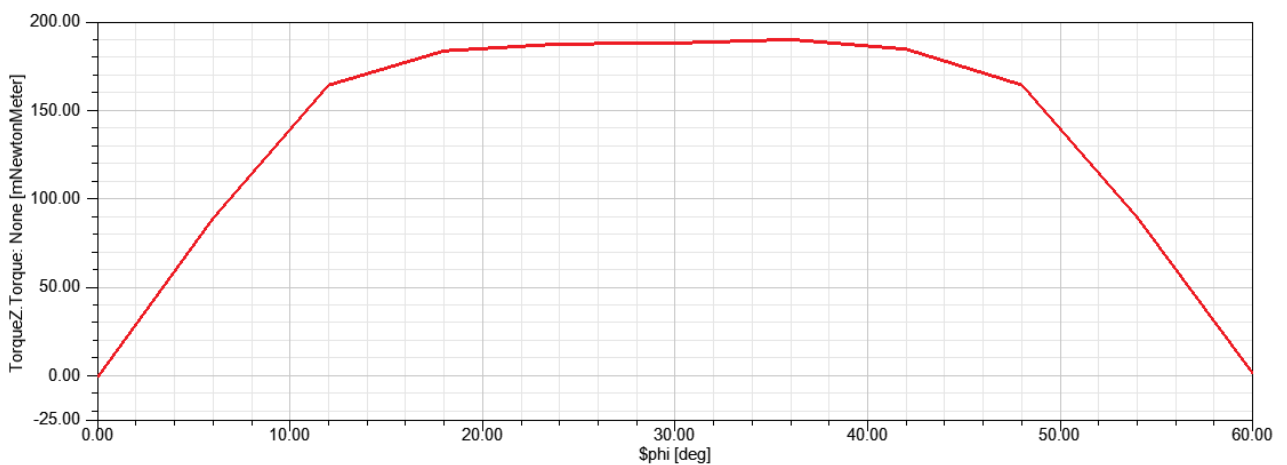
Figure 32 Torque with complete set of coil

5.4 TILTING TORQUE

The graphs in this section show tilting torque values when a single set of tilting coil is excited, for various angular positions of the rotor and values of the exciting current.
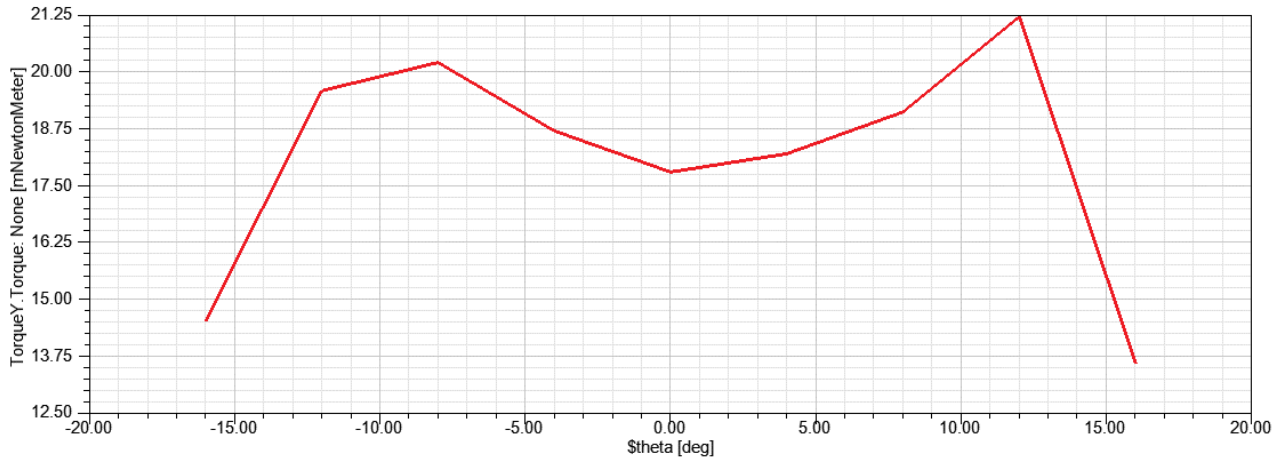
Figure 33 T_y when varying θ

6 VARIATIONS CONSIDERED

6.1 IRON CORE

Figure X shows the variation in B_r when considering a spherically shaped iron core positioned at centre of the rotor. While the difference in B_r is significant, the coreless configuration was chosen to keep the rotor lightweight.
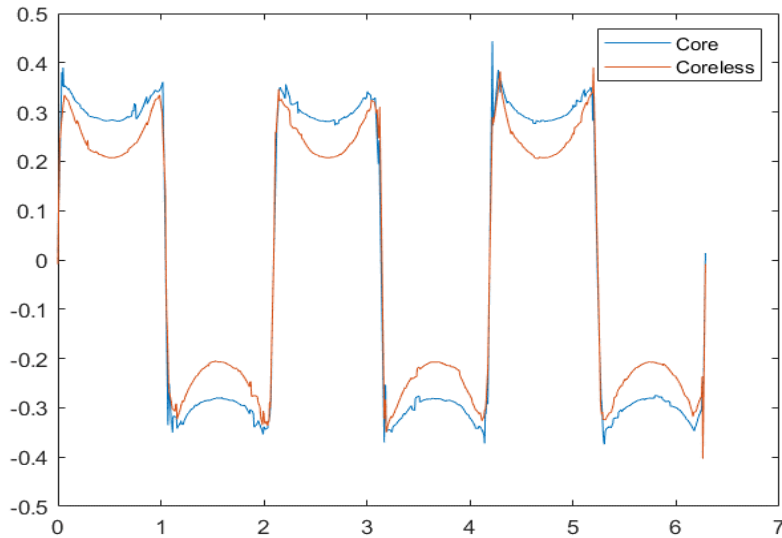
Figure 34 B_r comparison between air core and iron core

6.2 EQUATORIAL MAGNETS THICKNESS

Figure X presents the variation of the radial component of the magnetic field B_r, as calculated by the magnetic charge model, when the thickness of the permanent magnet is changed. It's clear that thicker permanent magnets provide a stronger magnetic field while thinner ones produce weaker ones.
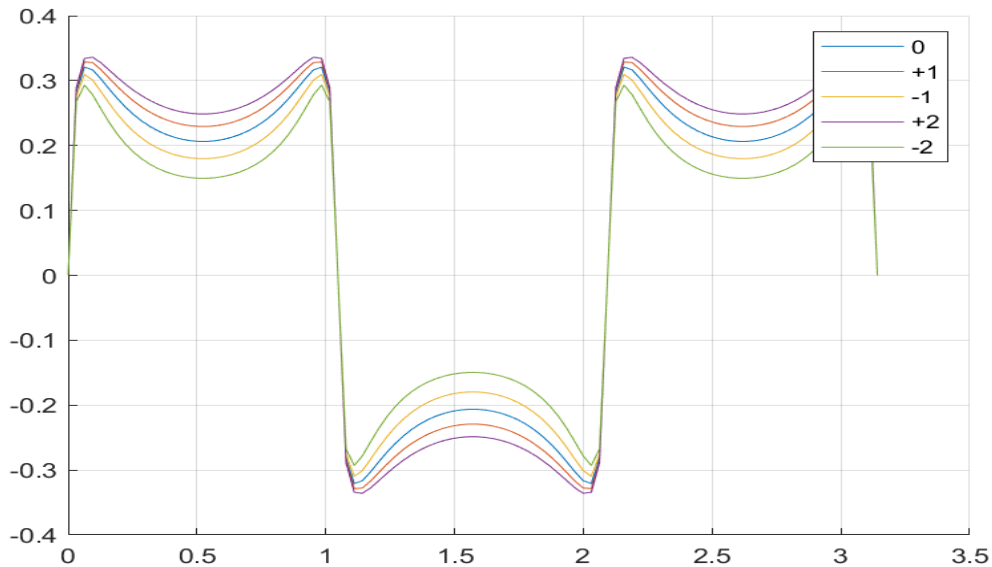
Figure 35 B_r for different PM thicknesses (from 4 to 8mm, 0 value at 6mm)

6.3 STATOR COIL LAYOUT

6.3.1 Disk Coils

This layout uses 6 disk shaped coils evenly spaced around the z-axis.
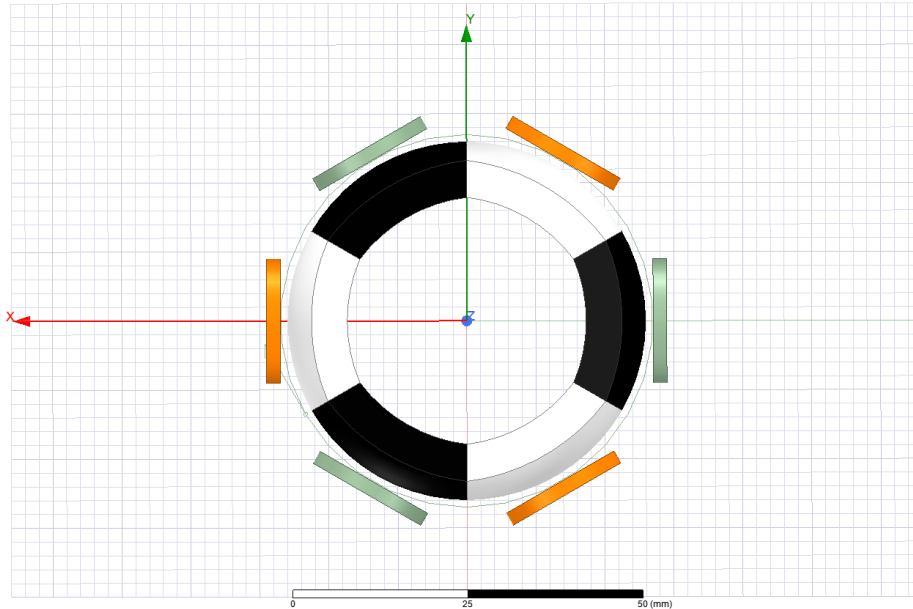
Figure 36 Actuator model with disk-shaped coils
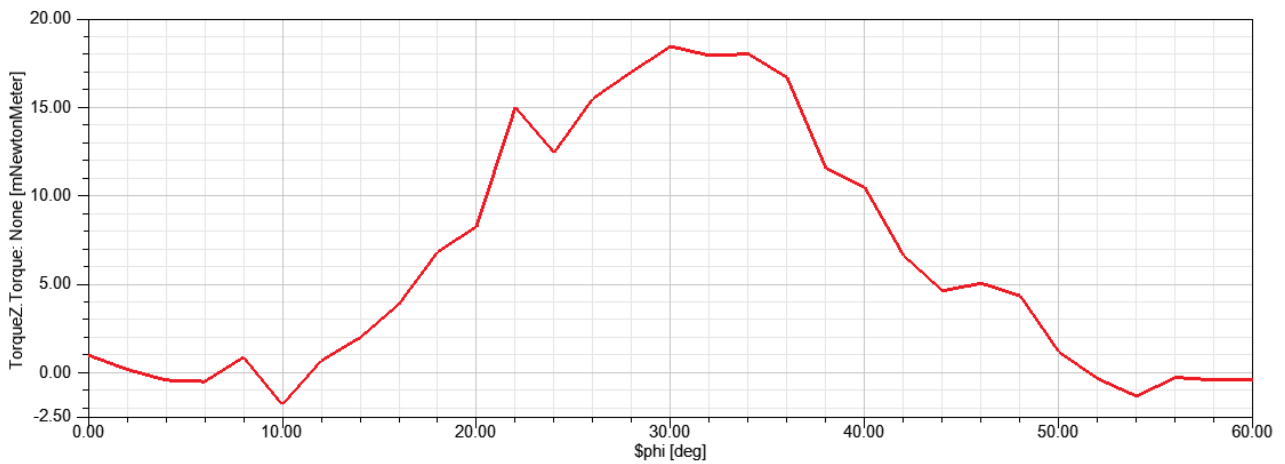
Figure 37 Spinning torque with disk coils

Note how the spinning torque obtained in this configuration quickly drops off outside the maximum torque position. This is due to the increase in air gap between the coil and the permanent magnets, as the coil does not follow the curvature of the permanent magnets.

6.3.2   Close Coils

This layout presents 6 coils evenly spaced around the z-axis of the rotor. The coil is shaped to follow the shape of the outer surface of the permanent magnets as close as possible.
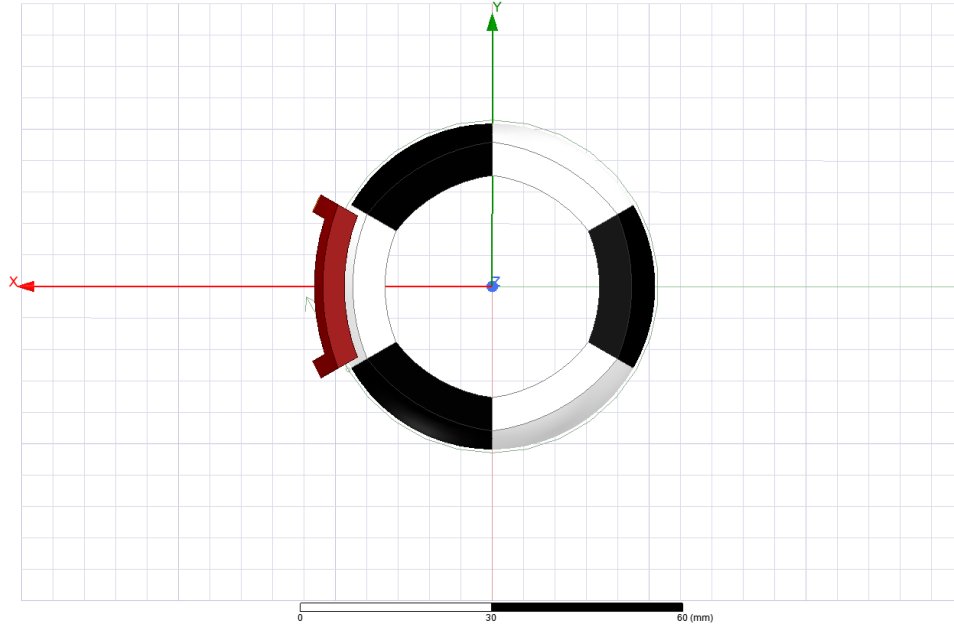
Figure 38 Rotor model with close fitting coil
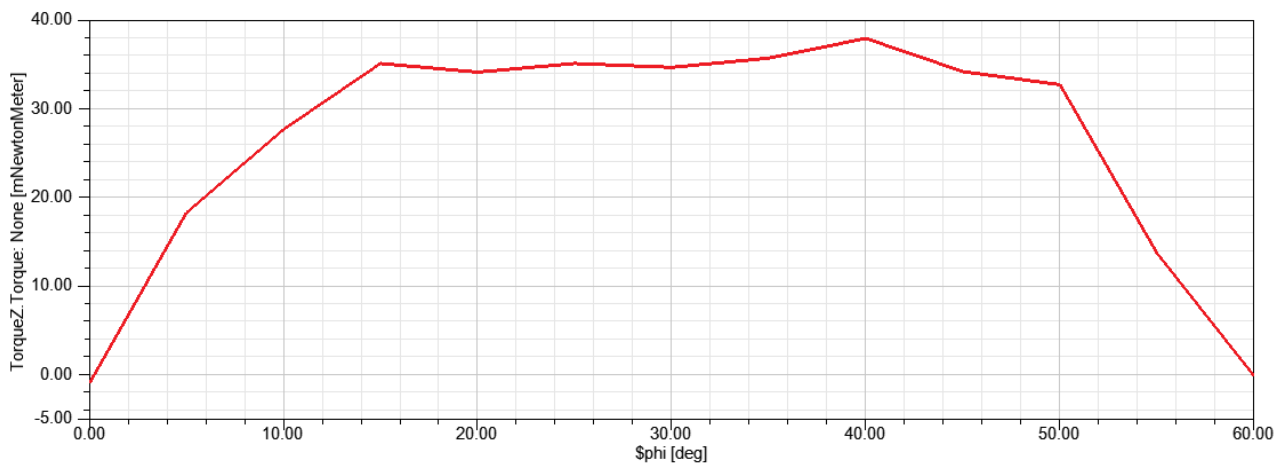
Figure 39 Spinning torque with close fitting coil

This configuration shows a wide range of almost constant T_z since air gap is constant.

6.3.3   Far Coils

The coils in this layout are shaped to have two active vertical sides, placing the horizontal ones far enough that their interactions with the permanent magnets is negligible.
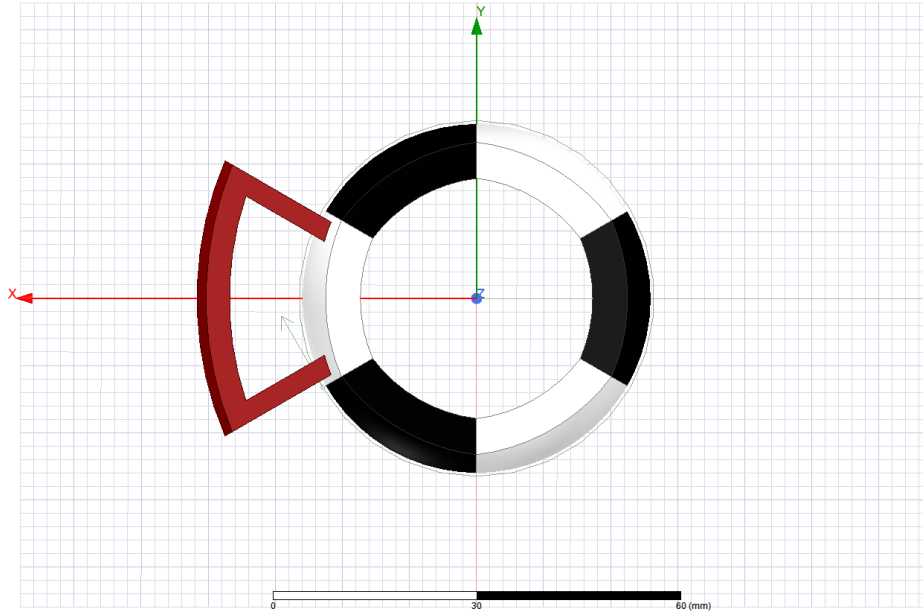
Figure 40 Actuator model with "far" coils
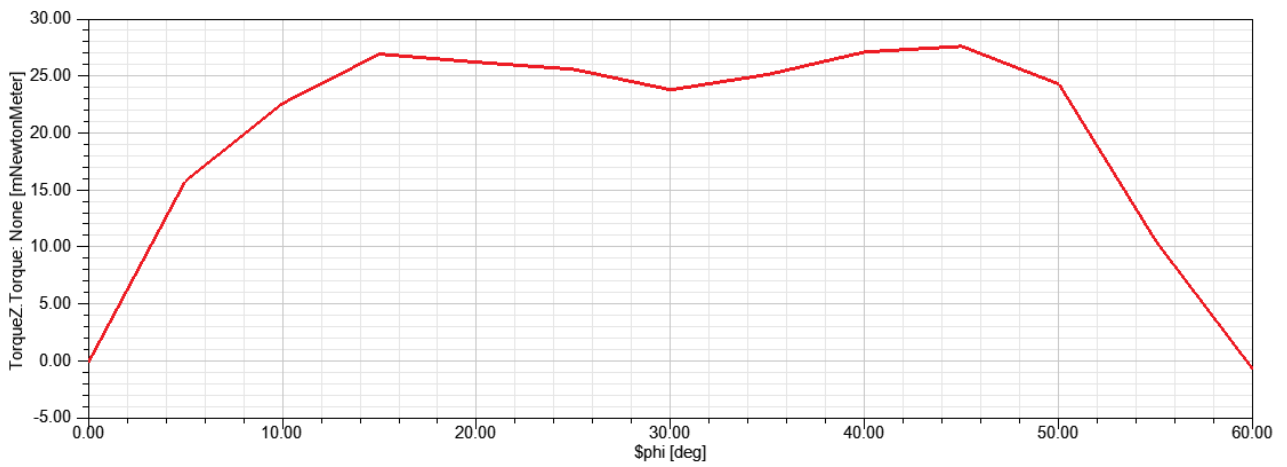
Figure 41 Spinning torque with "far" coils

6.3.4 Comparison

The graph in Image shows the spinning torque achieved by each of the previous three configurations when only one coil is excited with the same current [i][A*turns]
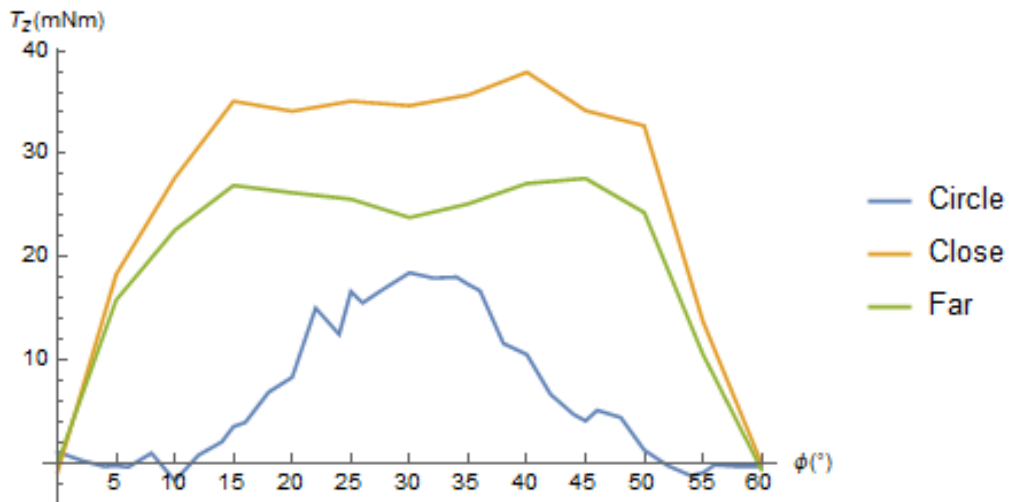
Figure 42 Comparison between coil layouts

Notice how both "Far" and "Close" have a wider range in which they produce torque, due to better following the shape of the rotor.
The configuration "Close" is the better performing of the three and is the one chosen in this work.

7 CONCLUSIONS

Actuators capable of performing spherical motions are increasingly used in industry thanks to their applications in areas such as robotics and advanced manufacturing.

In this work, an overview of spherical motor generators was presented, especially with regards to spherical permanent magnet actuators, along with modelling techniques for the magnetic flux density field.

After the overview, a design of spherical permanent magnet actuator is presented that can achieve rotation on all three axes.

Spherical harmonic, magnetic equivalent charge and FEM models were then used in the computation of the magnetic field of the designed spherical PM actuator. The spherical harmonic model was implemented in Mathematica, the magnetic equivalent charge model was implemented in both Mathematica and MatLab, but the MatLab one was used for the final calculations as its numerical integrator is faster. Finally, the FEM model was developed with Ansys Maxwell.

The models show good agreement with each other, but the spherical harmonic model needs a higher number of harmonics to be taken in consideration when performing the calculation, increasing its computational cost.

FEM simulations show that a significant rotational torque can be achieved, while tilting torque is much lower but still acceptable. Compared to other designs in literature, the torque produced is lower, but the structure is smaller and doesn't contain ferromagnetic components.

Some design variations were explored, particularly regarding the stator coils responsible for the spinning motion. Out of the three coil designs compared, although the shape is more complex than other solutions, the one with the highest spinning torque is chosen, as its torque also stays higher in a wider angular range.

8   APPENDIX – CODE

8.1   NBR.M

Numerically solves the integrals to calculate the radial component of the magnetic flux density field B_r by the magnetic charge equivalent method in a given position.

```matlab
function [br] = nBr(i,r,t,p)
  mu0 = pi*4e-7;
  M0 = -8.38e5;

  r1 = 20e-3;
  r2 = 26e-3;
  pI = deg2rad([0, 60, 120 , 180, 240, 300]);
  pF = pI + deg2rad(60);
  tI = deg2rad(60);
  tF = deg2rad(120);


  vol = @(rp,tp,pp) (-1).^(i-1).*(M0.*mu0.*rp.*sin(tp).*(-
r+rp.*cos(t).*cos(tp)+rp.*cos(p-pp).*sin(t).*sin(tp)))./ ...
    (2.*pi)./((r.^2+rp.^2-2.*r.*rp.*(cos(t).*cos(tp)+cos(p-
pp).*sin(t).*sin(tp)))).^(3/2);

  surf1 = @(tp,pp) (-1).^(i-1).*(M0.*mu0.*r1^2.*sin(tp).*(-
r+r1.*cos(t).*cos(tp)+r1.*cos(p-pp).*sin(t).*sin(tp)))./ ...
    (4.*pi)./((r.^2+r1^2-2.*r.*r1.*(cos(t).*cos(tp)+cos(p-
pp).*sin(t).*sin(tp)))).^(3/2);

  surf2 = @(tp,pp) (-1).^(i-1).*(M0.*mu0.*r2^2.*sin(tp).*(-
r+r2.*cos(t).*cos(tp)+r2.*cos(p-pp).*sin(t).*sin(tp)))./ ...
    (4.*pi)./((r.^2+r2^2-2.*r.*r2.*(cos(t).*cos(tp)+cos(p-
pp).*sin(t).*sin(tp)))).^(3/2);

  nsu1 = integral2(surf1, tI,tF, pI(i),pF(i));
  nsu2 = integral2(surf2, tI,tF, pI(i),pF(i));
  nvol = integral3(vol, r1,r2, tI,tF, pI(i),pF(i));

  br = -nsu1+nsu2-nvol;
end
```

8.2 NUMERICALCHARGE.M

Use the magnetic charge equivalent model to graph B_r on the equator and also obtain a 3D graph.

```matlab
disp('Section 1')
clear
pp = linspace(0,2*pi);
bi = zeros(length(pp),1);
br = bi;

for i=1:6
  j = 1;
  for p=pp % calculate the value around the equator for the
i-th magnet
    bi(j) = nBr(i,26.5e-3,pi/2,p);
    j = j+1;
  end
  br = br+bi; % sum the field due to each magnet
(superposition)
end

save('numericalcharge.mat', 'pp', 'br')
plot(pp, br)

%%
disp('Section 2');
clear
close
redo = true;
if isfile('numericalcharge3D.mat') && ~redo
  disp('using saved distribution...');
  load('numericalcharge3D.mat')
else
  disp('recalculating...');
  pp = linspace(0, 2*pi,42);
  tt = linspace(0, pi,21);
  bi = zeros(length(pp),length(tt));
  br3D = bi;

  for i=1:6
    j = 1;
    for p=pp
      k = 1;
      for t=tt
        bi(j,k) = nBr(i,26.5e-3,t,p);
        k = k+1;
      end
      j = j+1;
    end
```

```matlab
            br3D = br3D +bi;
        end

        save('numericalcharge3D.mat', 'pp', 'tt','br3D')
        disp('saved distribution to file');
    end
[X,Y] = meshgrid(rad2deg(tt),rad2deg(pp));
surf(X,Y,br3D,'FaceColor','interp')
xlabel('\theta [°]')
ylabel('\phi [°]')
zlabel('B_r [T]')
axis([0 180 0 360 -0.6 0.6])
colorbar
```

8.3 ACTSPHERICAL.M

Compare Magnetic Equivalent Charge and FEM models.

```matlab
th1=deg2rad(60);
th2=deg2rad(120);
ph1=deg2rad(0);
ph2=deg2rad(60);
r1 = 20e-3;
r2 = 26e-3;
lenBrFEA = csvread('./brHor.csv',1,0);
len = lenBrFEA(:,2);
BrFEA = lenBrFEA(:,3);
x = len;
br = zeros(length(x),1);
for i=1:length(x) % loop unrolling
    p=x(i);
    br2 = 0;
    br2 = br2 + -1 * nBr(26.5e-3, pi/2, p, r1,r2, th1,th2,
(0)*ph2,1*ph2);
    br2 = br2 + nBr(26.5e-3, pi/2, p, r1,r2, th1,th2,
(1)*ph2,2*ph2);
    br2 = br2 + (-1) * nBr(26.5e-3, pi/2, p, r1,r2, th1,th2,
(2)*ph2,3*ph2);
    br2 = br2 + nBr(26.5e-3, pi/2, p, r1,r2, th1,th2,
(3)*ph2,4*ph2);
    br2 = br2 + (-1) * nBr(26.5e-3, pi/2, p, r1,r2, th1,th2,
(4)*ph2,5*ph2);
    br2 = br2 + nBr(26.5e-3, pi/2, p, r1,r2, th1,th2,
(5)*ph2,6*ph2);
    br(i) = br2;
end
plot(x,br,len,BrFEA);
grid on;
legend('CRG','FEM')
```

8.4 VARTHICKNESS.M

Calculate B_r for differing PM thickness with MCM.

```
th1=deg2rad(60);
th2=deg2rad(120);
ph1=deg2rad(0);
ph2=deg2rad(60);

r2 = 26e-3;
thickness = 6e-3;
r1 = r2-thickness;

x = linspace(0,2*pi);
br = zeros(length(x),5);
for j=1:5
  if j==2
      r1 = r2-thickness-1e-3;
  elseif j==3
      r1 = r2-thickness+1e-3;
  elseif j==4
      r1 = r2-thickness-2e-3;
  elseif j==5
      r1 = r2-thickness+2e-3;
  end
  for i=1:length(x) % loop unrolling
    p=x(i);
    br2 = 0;
    br2 = br2 + -1 * nBr(26.5e-3, pi/2, p, r1,r2, th1,th2,
(0)*ph2,1*ph2);
    br2 = br2 + nBr(26.5e-3, pi/2, p, r1,r2, th1,th2,
(1)*ph2,2*ph2);
    br2 = br2 + (-1) * nBr(26.5e-3, pi/2, p, r1,r2, th1,th2,
(2)*ph2,3*ph2);
    br2 = br2 + nBr(26.5e-3, pi/2, p, r1,r2, th1,th2,
(3)*ph2,4*ph2);
    br2 = br2 + (-1) * nBr(26.5e-3, pi/2, p, r1,r2, th1,th2,
(4)*ph2,5*ph2);
    br2 = br2 + nBr(26.5e-3, pi/2, p, r1,r2, th1,th2,
(5)*ph2,6*ph2);
    br(j,i) = br2;
  end
end
plot(x,br(1,:),x,br(2,:),x,br(3,:),x,br(4,:),x,br(5,:));
grid on;
legend('0','+1','-1','+2','-2')
```

8.5 SPHERICAL.NB

Calculate B_r by spherical harmonics method.

```
μ0 = 4π*10-7; μm = 1.1;
M0=-8.38*10^5;
Num = 6; (* Num of magnets *)
p∈Range[1,Num];
(*$Assumptions = {-α/2+λ < φ<α/2+λ,  π/2-β <θ<π/2+β};*)
Rr = 26*10-3;Rb= 20*10-3;
α=N[60°];β=N[30°];
λ[p_]:=  2π (p-1)/Num;


Cnk[p_,n_,k_]:=Integrate[M0*(-1)p-1*Cos[pp-
λ[p]]SphericalHarmonicY[n,k,tt,pp]*Sin[tt]2, {pp,λ[p] ,α+λ[p]
},{tt, π/2-β ,π/2+β}];


dxia[n_]:=Rrn+2+(μm (2 n+1) Rbn+2 Rr2 n+1)/(n (μr-
μm) Rb2 n+1-Rr2 n+1 Abs[(n+1) μm+n μr]);


dshang[n_]:=(μm (2 n+1) (Abs[μr n+μm (n+1)] Rr2 n+1))/(n (μr-
μm) Rb2 n+1-Rr2 n+1 Abs[(n+1) μm+n μr])+(μm-1) (n+1);


d[n_]:=-(dxia[n]/dshang[n]);


ξ[p_,n_,k_]:=Cnk[p,n,k]*d[n];


Φ[p_,n_,k_]:=ξ[p,n,k]*SphericalHarmonicY[n,k,θ,φ]*r-
(n+1);(* +ξ[p,n,-k]*SphericalHarmonicY[n,-k,θ,φ]*r^-(n+1);*)


Brp[p_,n_,k_]  := -μ0*D[Φ[p,n,k],r];


xx = Table[φ,{φ,0,2π,π/30}];
yy = Table[Sum[Brp[p,3,3],{p,1,Num}]]/. {θ->N[90°],r->26.5*10-
3},{φ,0,2π,π/30}];
ListLinePlot[Transpose[{xx,Re[yy]}],Ticks->{Range[0°,360°,30°
],Automatic}]


Export["C:\\Users\\stisa\\OneDrive\\Universita\\Quinto Anno\\
ThesisM\\spr.csv",N[Transpose[{xx,Re[yy]}]],"CSV"]
```

9 FIGURES

10 REFERENCES

[1]   S. Bai, X. Li, and J. Angeles, "A review of spherical motion generation using either spherical parallel manipulators or spherical motors," *Mech. Mach. Theory*, vol. 140, pp. 377–388, 2019.

[2]   K. Takemura, S. Park, and T. Maeno, "Control of multi-dof ultrasonic actuator for dexterous surgical instrument," *J. Sound Vib.*, 2008.

[3]   T. Mashimo, S. Toyama, and H. Ishida, "Design and implementation of spherical ultrasonic motor," *IEEE Trans. Ultrason. Ferroelectr. Freq. Control*, 2009.

[4]   S. E. Wright, A. W. Mahoney, K. M. Popek, and J. J. Abbott, "The Spherical-Actuator-Magnet Manipulator: A Permanent-Magnet Robotic End-Effector," *IEEE Trans. Robot.*, vol. 33, no. 5, pp. 1013–1024, Oct. 2017.

[5]   H. Nagasawa and S. Honda, "Development of a Spherical Motor," pp. 2–5.

[6]   L. Gan, Y. Pei, and F. Chai, "Tilting Torque Calculation of a Novel Tiered Type Permanent Magnet Spherical Motor," *IEEE Trans. Ind. Electron.*, vol. 67, no. 1, pp. 421–431, 2019.

[7]   B. Van Ninhuijs, T. E. Motoasca, B. L. J. Gysen, and E. A. Lomonova, "Modeling of spherical magnet arrays using the magnetic charge model," *IEEE Trans. Magn.*, vol. 49, no. 7, pp. 4109–4112, 2013.

[8]   D. M. Healy, D. N. Rockmore, P. J. Kostelec, and S. Moore, "FFTs for the 2-Sphere-Improvements and Variations," *J. Fourier Anal. Appl.*, vol. 9, no. 4, pp. 341–385, 2003.

[9]   L. Yan, I.-M. Chen, C. K. Lim, G. Yang, and K.-M. Lee, "Design, Modeling and Experiments of 3-DOF Electromagnetic Spherical Actuators (Mechanisms and Machine Science)," pp. 29–47, 2011.

[10]   L. Yan, I. M. Chen, H. Son, C. K. Lim, and G. Yang, "Analysis of pole configurations of permanent-magnet spherical actuators," *IEEE/ASME Trans. Mechatronics*, vol. 15, no. 6, pp. 985–989, 2010.

[11]   L. Yan, D. Liu, Z. Jiao, C. Y. Chen, and I. M. Chen, "Modeling of magnetic field and design optimization for permanent-magnet spherical actuator in three dimensional space," *Proc. 2015 10th IEEE Conf. Ind. Electron. Appl. ICIEA 2015*, pp. 1904–1909, 2015.

[12]   Z. Li, L. Zhang, and Q. Q. Lun, "Modeling and Optimized Design of a New Multi-DOF Deflection Type PM Motor," *Adv. Mater. Res.*, vol. 951, pp. 67–70, 2014.

[13]   Z. Li, C. Wang, Q. Lun, and L. Zhang, "Design and electromagnetic analysis of a novel 3-DOF deflection type permanent magnet actuator," *2014 IEEE Transp. Electrif. Conf. Expo*, pp. 1–6, 2014.

[14]   Z. Li and Q. Q. Lun, "Analysis of magnetic field and levitation force characteristics for 3-DOF deflection type PM motors," *J. Chinese Inst. Eng. Trans. Chinese Inst. Eng. A/Chung-kuo K. Ch'eng Hsuch K'an*, vol. 39, no. 6, pp. 704–712, 2016.

[15]   S. Ahmadi, J. S. Moghani, and M. Mirsalim, "Simulation and analysis of a novel PM spherical 3-DOF actuator with E-shaped stator and blade-shaped rotor structure," *9th Annu. Int. Power Electron. Drive Syst. Technol. Conf. PEDSTC 2018*, vol. 2018-Janua, pp. 59–64, 2018.

[16]   M. J. Sidi, *Spacecraft dynamics and control: A practical engineering approach*. 2014.

[17]   L. Rossini, S. Mingard, A. Boletis, E. Forzani, E. Onillon, and Y. Perriard, "Rotor design optimization for a reaction sphere actuator," *IEEE Trans. Ind. Appl.*, 2014.

[18]   L. Rossini, E. Onillon, O. Chetelat, and Y. Perriard, "Hybrid FEM-analytical force and torque models of a reaction sphere actuator," *Proc. 2013 IEEE Int. Electr. Mach. Drives Conf. IEMDC 2013*, pp. 694–

700, 2013.

[19]   L. Rossini, O. Chetelat, E. Onillon, and Y. Perriard, "Force and torque analytical models of a reaction sphere actuator based on spherical harmonic rotation and decomposition," *IEEE/ASME Trans. Mechatronics*, vol. 18, no. 3, pp. 1006–1018, 2013.

[20]   L. Yan, I.-M. Chen, C. K. Lim, G. Yang, and K.-M. Lee, *Design, Modeling and Experiments of 3-DOF Electromagnetic Spherical Actuators*, vol. 4. Dordrecht: Springer Netherlands, 2011.

[21]   H. Kim, H. Kim, and D. Gweon, "Magnetic field analysis of a VCM spherical actuator," *Sensors Actuators, A Phys.*, vol. 195, pp. 38–49, 2013.

[22]   Ansys and Inc, "ANSYS Maxwell Magnetic Field Formulation," pp. 1–3, 2013.

[23]   Ansys, "Maxwell Help," no. April, 2018.